Passive Devices in Silicon Photonics & their Automated Measurements

Amar Kumar

Department of Electrical & Computer Engineering
McGill University
Montreal, Canada

December 2019

A thesis submitted to McGill University in partial fulfillment of the requirements for the degree of Master of Engineering.

Abstract

Silicon has become a popular platform for the integration of a large number of devices. The material property of silicon and its high contrast in refractive index with silica makes it a preferable choice for smaller devices. This thesis has a detailed analysis of two significant passive devices, namely - grating couplers and Y-branch. A grating coupler enables an efficient way of coupling light from the free space to the circuit. It is an on-chip coupling solution besides other complicated techniques such as edge coupling or butt coupling. An efficient design of grating coupler with low loss, low back reflection and high 1 dB bandwidth is efficient and easier to implement compared to other techniques as it reduces the complexity of optics. The best grating coupler design presented in this thesis has a measured insertion loss of -4.95 dB and 1 dB bandwidth of 93 nm.

Using conventional techniques for designing a silicon photonic passive device at times proves to be cumbersome because converging to an optimized solution might be difficult. Therefore a robust algorithm with a better optimization technique is necessary. A method of designing efficient Y-branch using particle swarm optimization is discussed in detail in this thesis. The fabricated devices are quick to design and their performance is usually better than the conventional devices. The Y-branch designed using this technique has a 50-50 splitting over the entire wavelength range of 1500 nm - 1600 nm. The technique of using a particle swarm algorithm can further be extrapolated to other algorithms like gradient descent or machine learning for designing more complicated devices.

Finally, this work also presents the design of an automated stage for testing passive devices. The stage is fully capable of aligning fibers to a passive device and perform its characterization. This system increases the efficiency of measurement by 60 times, thereby reducing the time required to couple the light and align the chip. Rapid interpolation algorithms are used to find the optimized position given an objective function.

Abstraite

Le silicium est devenu une plate-forme populaire pour l'intégration d'un grand nombre d'appareils. La propriété matérielle du silicium et son contraste élevé d'indice de réfraction avec la silice en font un choix préférable pour les petits appareils. Cette thèse présente une analyse détaillée de deux dispositifs passifs importants, à savoir - les coupleurs à réseau et la branche Y. Un coupleur à réseau permet de coupler efficacement la lumière de l'espace libre au circuit. Il s'agit d'une solution de couplage sur puce en plus d'autres techniques compliquées telles que le couplage de bord ou le couplage bout à bout. Une conception efficace de coupleur à réseau à faible perte, à faible réflexion arriére et à large bande passante de 1 dB est efficace et plus facile à mettre en œuvre par rapport à d'autres techniques car elle réduit la complexité de l'optique. La meilleure conception de coupleur de réseau présentée dans cette thèse a une perte d'insertion mesurée de -4.95 dB et une bande passante de 1 dB de 93 nm.

L'utilisation de techniques conventionnelles pour concevoir un dispositif passif photonique au silicium se révèle parfois fastidieuse car la convergence vers une solution optimisée peut être difficile. Par conséquent, un algorithme robuste avec une meilleure technique d'optimisation est nécessaire. Une méthode de conception d'une branche Y efficace utilisant l'optimisation de l'essaim de particules est discutée en détail dans cette thèse. Les appareils fabriqués sont rapides à concevoir et leurs performances sont généralement meilleures que les appareils conventionnels. La branche Y conçue à l'aide de cette technique a une division de 50 à 50 sur toute la gamme de longueurs d'onde de 1500 nm à 1600 nm. La technique d'utiliser un algorithme d'essaim de particules peut en outre être extrapolé à d'autres algorithmes comme la descente de gradient ou l'apprentissage automatique pour concevoir des dispositifs plus compliqués.

Enfin, ce travail présente également la conception d'une étape automatisée pour tester des dispositifs passifs. La platine est parfaitement capable d'aligner les fibres sur un appareil passif et d'effectuer sa caractérisation. Ce système augmente l'efficacité de la mesure de 60 fois, réduisant ainsi le temps nécessaire pour coupler la lumiére et aligner la puce. Des algorithmes d'interpolation rapide sont utilisés pour trouver la position optimisée en fonction d'une fonction objectif.

Acknowledgments

I would like to sincerely thank my supervisor, Prof. David V. Plant for his constant support, instructions and pieces of advice throughout my research work and graduate studies at McGill in general. Prof. Plant's utmost dedication and efforts have provided us (Plant Group) with the best and unparalleled laboratory facilities in Canada and worldwide. The high-end equipments and tools that we have in our lab have helped me and other researchers in our group as well as to have impactful results on current technologies in optical communication and silicon photonics. I feel deeply honoured to pursue my graduate research under his supervision.

I would also like to thank Prof. Lawrence R. Chen whose course 'Photonics Devices and Application' helped me develop an in-depth understanding of Silicon Photonic devices. Next, I would like to thank Prof. Lukas Chrostowski whose online course gave me a deeper insight into using different simulation tools for designing photonic circuits. His course also provided me with immense details on using exact drawing tools for designing the layout used in fabrications. I would also like to extend my thanks to Prof. Andrew J. Kirk whose course 'Optical Engineering' provided me with greater insight into optics and its design techniques.

I would also like to thank my colleague Dr. Yun Wang, who helped me initially with the simulations and idea for the thesis. Yannick D' Mellow, who helped me write some parts of the code for automated setup. Eslam Elfiky, Maxime Jacques, Md. Saber Gulam, Heba Tamazin, Deng Mao, Luhua Xu, Michael Hui who helped me with various codes, debugging and laboratory equipments. I would also like to thank my colleague Md. Samiul Alam for his help and support. Working in the lab was more fun because of such helpful people around.

Finally, all this was possible because of my family. I would also like to give special thanks to my father - Ghanshyam; mother - Bandani; sister - Juhi and brother - Ashutosh for their deepest love, care and support. I would also like to thank my dear friend, Ankita for her help.

-*Amar*

Contents

List of Figures

List of Tables

List of Acronyms

BOX buried oxide

CE Coupling Efficiency

CMOS Complementary Metal-Oxide Semiconductor

DC directional coupler

ER Extinction Ratio

FAU Fiber Array Unit

FDTD Finite Difference Time Domain

FEM Finite Element Method

FOM Figure of Merit

GC Grating Coupler

GUI Graphical User Interface

IL Insertion Loss

LED Light Emitting Diode

MDM mode division multiplexing

MMI Multi-Mode Interferometer

MZM Mach Zehnder Modulator

PaNaMS Passive Nanophotonic Measurement System

PSO Particle Swarm Optimization

SiP Silicon Photonics

SMF single-mode fiber

SOI Silicon-on-insulator

SWGC Sub Wavelength Grating Coupler

TE Transverse Electric

TIR total internal reflection

TM Transverse Magnetic

PML perfectly matched layer

Chapter 1

Introduction

Electronics has become an integral part of our life with its applications ranging from automobiles, and entertainment media to internet and communications. There is increasing competition between the electronics and the photonics industry, and a merger of these two fields has resulted in the development of high-speed integrated devices [1, 2].

1.1 Silicon Photonics

Silicon is one of the most widely researched materials in semiconductor technology because of its properties and wide range of applicability in electronics. The introduction of silicon-based transistors has revolutionized the electronics industry, and today, millions of transistors are embedded on a single chip, thereby enhancing its space utilization capability. For example, the advanced fabrication capability of the Complementary Metal-Oxide Semiconductor (CMOS) transistor allows it to be as small as 20 nm. Additionally, the fabrication industries' continuous reduction in the feature size has enabled more devices on a small chip, with Moore's law describing its consequences. Silicon photonics deals with the making of optical devices by using silicon as a substrate and any combination of group III-IV or group IV-V elements, such as Si_3N_4 or SiO_2. These materials have the potential to make better device designs.
As a result, the requirements of higher data transfer speeds, low power consuming multi-core processors, and high output on-chip networks in the communication industry is difficult without SiP. Fig. 1.1 shows how the integration of SiP devices on-chip has the capability of performing high-speed data modulation.

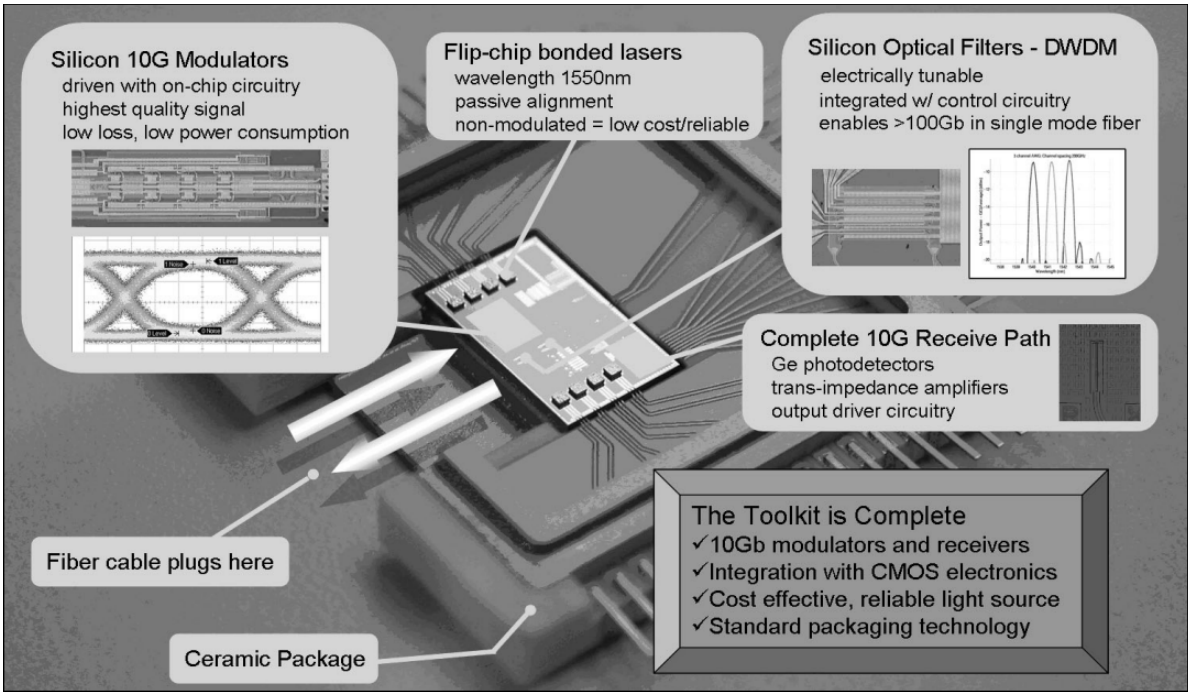

Fig. 1.1 A prototype of 10Gb/s transceiver from Luxtera corporation [3, 4]

Apart from communications, SiP is also relevant in the areas of sensing. For example, silicon ring resonators find application in optical scanning as bio-sensors [5], gyroscopes (application in cameras, automobiles, and the space industry) and silicon-based devices [6]. Fig. 1.2 shows the diversity of SiP and its applicability in the integration of optical interconnects. As compared to the CMOS industry, where devices are compact (14 nm [7] in size), the devices in SiP are as large as 60 nm due to restrictions imposed by its insertion loss, wavelength and design. A combination of materials like germanium and indium is used to bridge the gap between photonics and electronics. One of the standard applications of germanium-based devices is to convert a given intensity of the light to the electric current using photodiodes [8, 9, 10]. Richard Soref [11] comments on some of the areas of application of photonics such as Raman lasers, photonic crystals, fast modulators, light-emitting diodes, photodetectors, microresonators, plasmon optics, quantum-cascade structures, and photonic-circuits integrations. According to him, the silicon industry has a bright future in the development of a true optoelectronic integration on CMOS in a stable 130 nm or 90 nm commercial process. These developments will result in fast, cost-effective optical interconnects of computer chips.

In the current scenario, silicon photonics also serves as the backbone of the optical components and communications industry. Companies like IBM, Intel and others deploy a

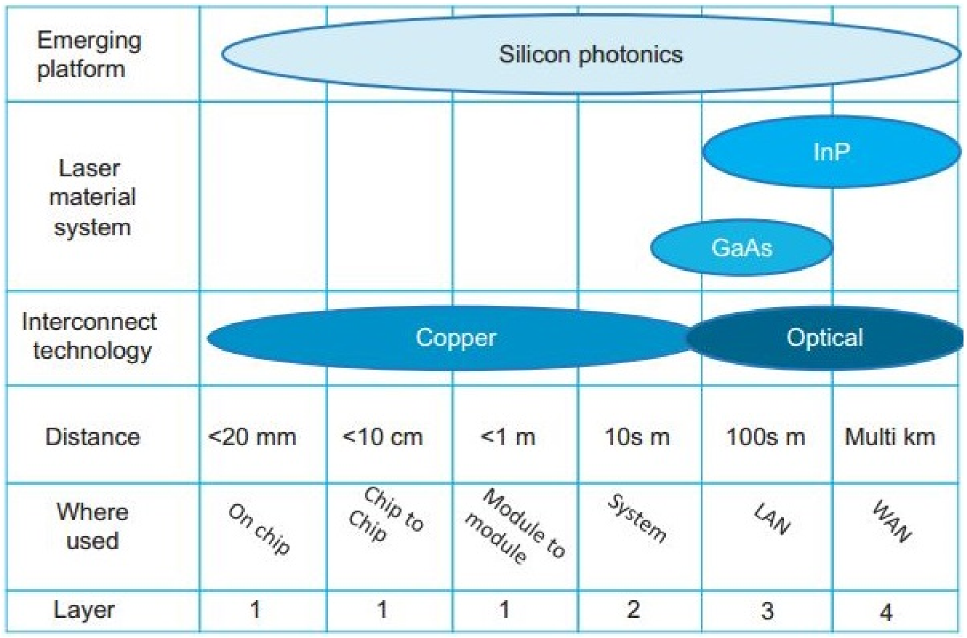

Fig. 1.2 Coverage of Silicon Photonics in different areas. The figure is taken from [12].

significant amount of resources for research and development in the field of silicon photonics. Fig. 1.3 shows future investments for the use of SiP in data centers as compared to other areas.

Fig. 1.4 shows a typical integrated silicon photonics chip with each part labeled in red. A laser operates as the primary light source in all the SiP devices. A detector (e.g., photodiode) on a SiP chip is a device that converts an optical signal to an electrical signal. A modulator like the Mach Zehnder Modulator (MZM) converts an electrical signal to an optical signal. Signals on the optical chip undergo basic operations of muxing and demuxing. Finally, all the optical signals are launched into the chip or received from it using coupling devices like edge couplers or grating couplers.
Silicon based optical interconnect components are categorized into passives and actives. Passive SiP devices, such as a Y-branch, grating coupler, and a Multi-Mode Interferometer (MMI), are purely optics-based and require no external modulation (external modulation in silicon is typically accomplished by a change in the effective index or a change in absorption)

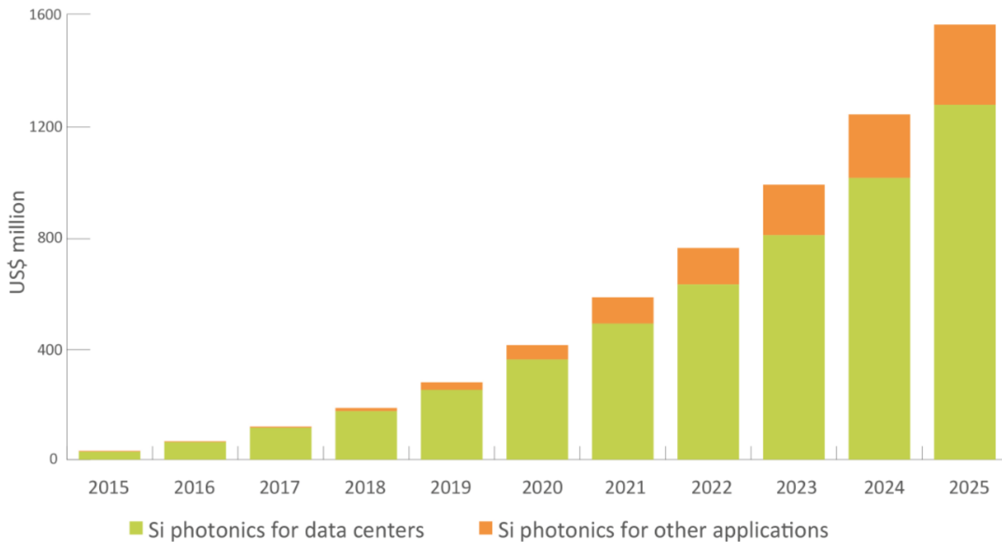

Fig. 1.3 Future investments in the SiP industry. *Source: Yole Développement.*

for their operations. Actives, on the other hand, require external modulation in order to work. These devices include modulators, switches, and photodetectors. Generally, heaters are placed closer to the waveguides in active devices for the manipulation of the refractive index profile of a material.

1.2 Passive Devices

Silicon-on-insulator (SOI) is an ideal platform for the development of passive optical components. Due to the optical transparency of silicon in the telecommunication window, low-loss guidance of light is achievable [13]. SiP passive devices have gained immense popularity because of their high performance, low IL, and compact structure. As a result of their low complexity and robustness, these devices are preferred in industrial-grade equipment. Some of the popular passive devices include a grating coupler, MMI, directional coupler (DC) and ring resonator. Designing the SiP passive devices has its challenges. For instance, in some of these devices, like the wavelength filters that have polarization dependence, the design criteria must be carefully considered.

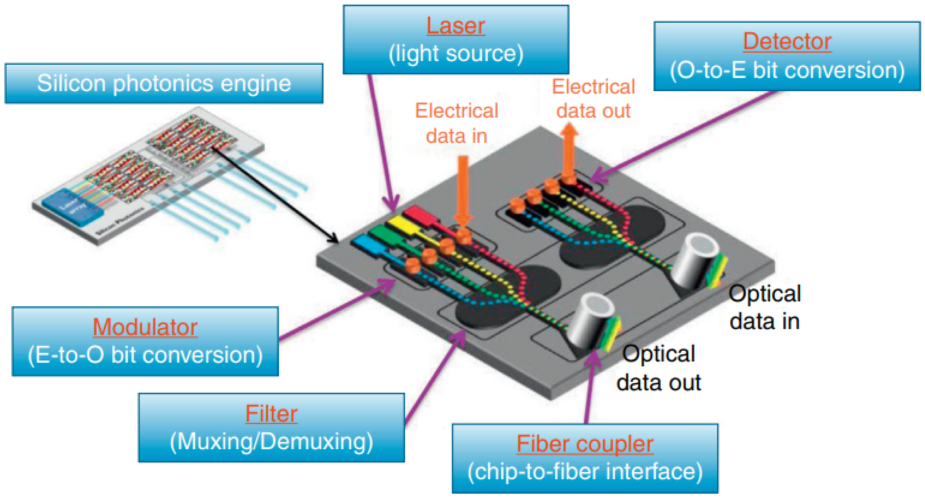

Fig. 1.4 An integrated silicon photonic chip. This picture is taken from [12].

1.3 Thesis Objective and Scope

In order to work with a SiP circuit, the light needs to be coupled into the chip with high efficiency. Later, the same light is diverted to various devices, depending on their purposes. This thesis aims to give a detailed insight into two passive SiP devices, the grating coupler, and the Y-branch, as well as elaborate upon their design, manufacturing, and testing on an SOI platform. The thesis also elucidates the design of an automated stage for measurement and testing of the SiP chips.

This thesis consists of five chapters.

Chapter 1 presents an introduction to silicon photonics and outlines the topics covered in this thesis.

Chapter 2 provides details of the PaNaMS, an automated system that performs measurements on the passive SiP devices, including the details of the system capabilities and its architecture. The chapter also elaborates upon future updates to the stage to enhance its capabilities.

Chapter 3 explores the theoretical aspects related to grating couplers along with details on the sub-wavelength structures used in the device. A difference in design by etching different regions of the grating coupler improves the performance. The chapter also discusses a new design of the sub-wavelength grating coupler along with measurement results.

Chapter 4 discusses the methods used for designing an optimized Y-branch using PSO. Such a design method along with the selection of an efficient Figure of Merit (FOM), can generate designs with high performance. The model used for creating the Y-branch is robust with low loss when measured. The end of the chapter provides a brief discussion on using a sophisticated algorithm to design the circuit. The technique uses bounded optimization and is extremely efficient.

Finally, the research work concludes in chapter 5, highlighting the critical aspects and key features of the manufactured passive devices.

Chapter 2

Design, Experimental Methods and Tests

This chapter discusses the design and functionalities of the automated stage, which is essential for measuring passive devices. This stage has the capability of carrying out measurements 60 times faster. Section 2.1 describes how to carry out measurements manually and elucidates the advantages of using an automated stage over manual alignments. Section 2.2 highlights the system architecture of the automated stage and the features of various components along with different connection protocols. Section 2.3 describes the alignment protocol and optimization used by the automated stage for making faster measurements. Finally, section 2.4 discusses different ways to upgrade and make it more user-friendly.

2.1 Introduction

Carrying out measurements on a passive SiP chip is a tedious task. Proper alignment of the grating coupler present on the chip requires significant effort, and even a slight misalignment of micrometers can cause immense insertion loss. For carrying out manual measurements of the grating coupler, the laser reaches the chip at a specific angle through FAU. The incident angle of the light is as per the design convention followed during simulations. The power detected at the other end of the grating coupler pair is monitored in real-time using any conventional detector. The movements are continuously made using a high-precision controlled stage to receive maximum power from the grating coupler at the output. The position at which the chip attains the maximum power is the optimized position. At this

position, one can record the output spectrum after carrying a wavelength sweep. The sweep range is selected based on the band of operation (i.e., C-band or O-band) of the device. If the peak of the obtained spectral response is closer to the expected central wavelength, the device is said to be aligned. If otherwise, the angle of incidence must be adjusted. For a grating coupler pair, the peak of the spectral response can shift about 6 nm for every change in the angle of incidence by a degree.
Furthermore, one needs to carry the same alignment in case any device whose insertion loss is to be measured and the corresponding required output spectrum is recorded. Finally, to obtain the insertion loss of the device, the spectral response of the device is subtracted from the spectral response of the grating coupler. This entire measurement for characterizing the IL of a passive SiP device takes about 12-20 minutes, depending on the expertise of the person recording the data. An automated passive measurement stage is created to carry out the same task at a quicker pace. Measurements of the same devices on the automated stage take around 15-20 seconds. The stage uses advanced aligning techniques to carry out rapid measurements. Apart from the algorithm, the speed also comes from the high-end hardware used. The name PaNaMS refers to the complete measurement system.

2.2 System Architecture

The complete system consists of the following equipment:

1. **Laser:** This system architecture uses a tunable laser with a wavelength range as per the band of operation of the device. This system architecture uses Yenista Tunics, which automatically connects to either CL-band or O-band lasers. However, additional drivers can be added to make it compatible with any laser. The O-band laser can perform a wavelength sweep from 1260 nm - 1360 nm, and the CL-band laser sweeps from 1500 nm - 1630 nm.

2. **Power detector:** A detector with four parallel channels where each channel measures power in the range 0 - 10 mW; currently, Yenista CT-400 is in use.

3. **Polarization Controller:** This applies mechanical stress to the fiber to change the state of polarization of the incident light launched into the device.

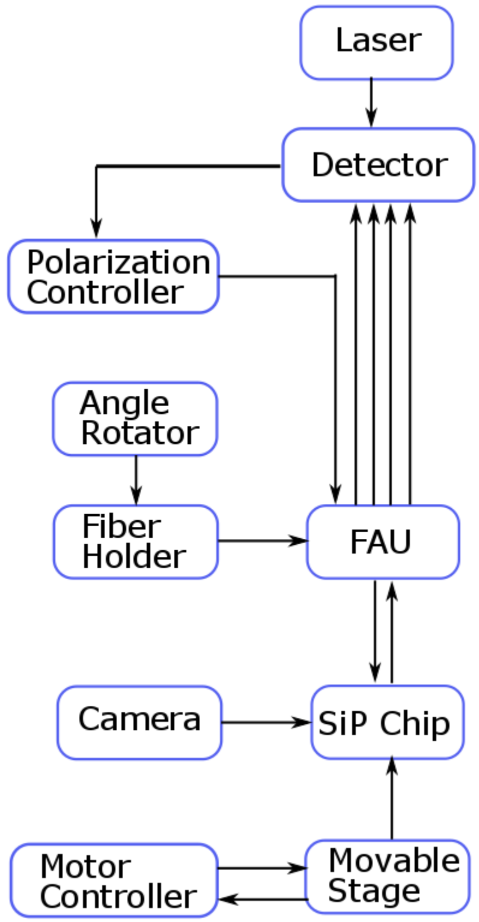

Fig. 2.1 Complete schematic of the PaNaMS.

4. **Translation stages:** These control the movement of the stage in the X and Y directions. The Z translation stage controls the position of FAU and determines the closeness of FAU to the chip. The X and Y-axes have feedback attached to the controller, which enables them to have the precise location of the stage. The user can adjust the position of the Z-axis, dependent upon the alignment of the chip, the nature of the device to be measured and the incident angle of the laser.

5. **Motor Controller:** This is used to control different axes of the stage. Currently, the system uses Corvus ECO, a high-precision motor controller with an accuracy of 1 μm.

6. **FAU**: The FAU has multiple fibers on a single strip and directs light to the chip. It

is attached to a fiber holder whose angle can be adjusted by an angle rotator. The FAU used for the experiment had 4 or 8 fibers and a spacing of 127 μm between consecutive fibers.

7. **Camera:** A standard camera with high resolution is used to show an image of the device under test. It ensures that while the measurement is being carried out, FAU is pointing to the correct device.

Fig. 2.1 shows a full representational model of the PaNaMS. The direction of the arrows indicates the input and output of various components. While the output from the laser goes into the detector, the output from the detector goes to the FAU through the polarization controller. The FAU has multiple fibers on a single strip. However, the output at only four ports can be detected simultaneously. So, one of the fiber ports of the FAU is used to launch light into the SiP chip while the other fiber ports collect the light returned from the device. The respective output ports are connected to the terminals of the detector. For instance, to test grating couplers, any one of the fibers in the FAU can be used as an input, while the fiber next to it (or at a multiple of 127 μm) is used as an output. The output port is connected to the detector while the other three ports of the detector are left empty. The SiP chip placed on the movable stage translates as per the stage. The motor controller checks the speed of the movable stage and provides feedback on the current position of the stage to the system. Fig. 2.2 shows all the different components of the PaNaMS.
The user needs to adjust the polarization controller carefully as changes in the state of the polarization affect the measured insertion loss of the device. Hence, to have the correct state of polarization of the device, reference grating couplers are placed on the chip. The spectral response and performance of these grating couplers are known in advance. Thus, before beginning the experiment, the polarization controller is tuned such that the user obtains the expected spectral response for the reference grating coupler. After the state of polarization has been determined, all the devices with a state of polarization similar to the reference grating coupler are measured. Therefore, the user must adjust the polarization controller after measuring a set of devices in order to shift to devices with a different state of polarization. For example, if a user aligns the polarization controller to the reference device with a Transverse Electric (TE) state, then after measuring all the TE devices, the user needs to switch the state of the polarization controller and readjust it according to a Transverse Magnetic (TM) reference grating coupler for measuring TM devices.

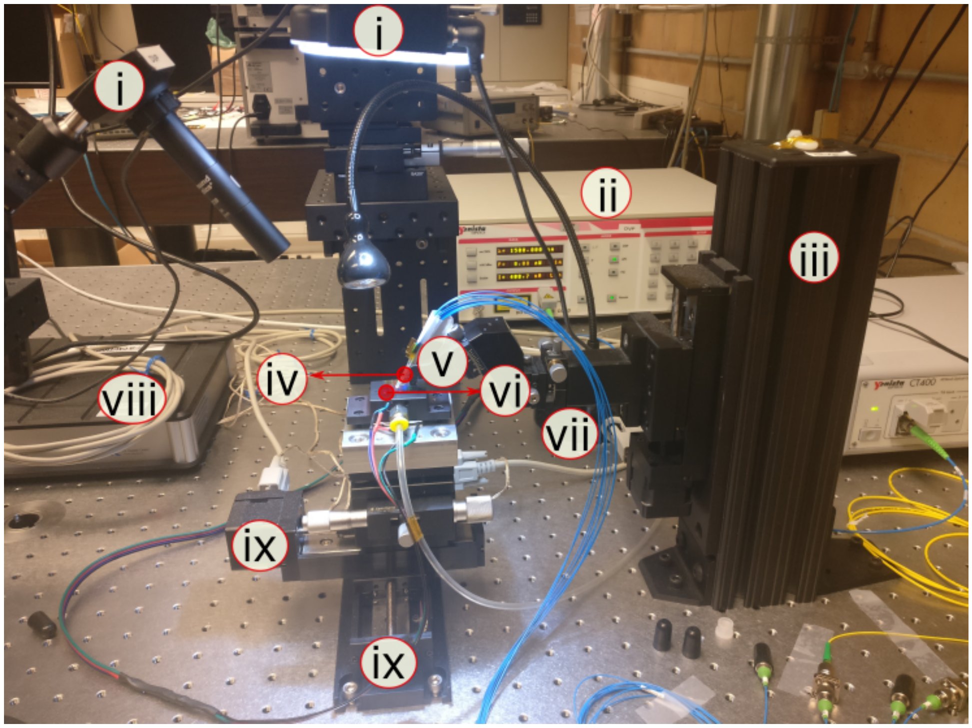

(a)

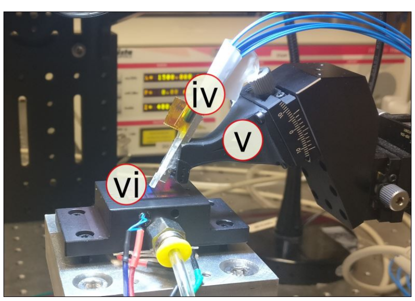

(b)

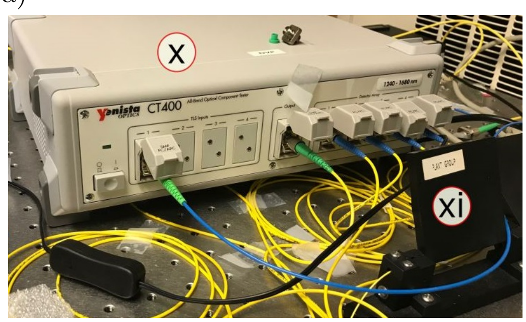

(c)

Fig. 2.2 All the components of a PaNaMS: (a) i-camera, ii-laser, iii-z-translation stage, iv-FAU, v-fiber holder, vi-chip, vii-angle rotator, viii-motor controller, and ix- x and y-translation stage, (b) a closer look at the chip, and (c) x - detector, and xi - polarization controller.

2.2.1 GUI for the PaNaMS

Fig. 2.3 shows the GUI and control of different functionalities. Panel 1 shows the controls for the laser. The user needs to select 'Load Library' and then press 'ON' in order to set up the connection to the laser. After a successful connection, the user can modify the wavelength and power. Depending upon the wavelength specified in this panel, the system automatically checks for the corresponding laser, and a successful connection is established if the laser is available. Panel 2 shows the sweep controls of the wavelength (in nm) from start to stop. The user can adjust the resolution, sweep speed and power. Panel 3 shows almost real-time power (there is a lag of 2-5 milliseconds) at various outputs of the device. Panel 4 shows the stage controls which hold the chip. The motor controller that handles the x and y-axes has feedback attached to it. On the other hand, the z-axis has motor controls without the encoder (i.e., feedback). The x and y display monitors show the positions based on the feedback. The 'Go' button alongside the position display allows the user to move to the specified location of the chip as entered. The 'Align' button orients the chip as per the settings. The 'On'/'Off' toggle button in panels 1, 3 and 4 controls the connection to the laser, detector, and motor, respectively. The green color in Fig. 2.3 shows a successful connection to these individual devices (a red color for the same button will denote an unsuccessful connection).

Fine alignment is a technique in which the chip is slightly moved in either direction to locate the optimized position. Fig. 2.4 shows different functionalities that can be adjusted while performing a fine alignment. The wavelength and power shown in the window determine the characteristic of the input light. The step size shown in Fig. 2.4 is the minimum distance specified by the user across two successive data points, and a scan window depicts the complete area to be scanned. The scan threshold, as depicted in Fig. 2.4 is the minimum power detected by the system to confirm that a device is found (i.e., light is coupled to the device). Selecting the option 'Done' saves the specified settings in the computer's memory. The 'Plot Spectrum' area shows the response obtained on the four parallel detectors of the device under testing. Users can select the checkboxes to plot a response from specific detector ports. Users can subsequently save the corresponding figure displayed in the 'Plot Spectrum' by inserting the path and the name of the file. The spectrum plot in Fig. 2.3 shows the response of a back-to-back grating coupler on one channel of the detector and noise on the other three channels. The spectrum was obtained by connecting the output

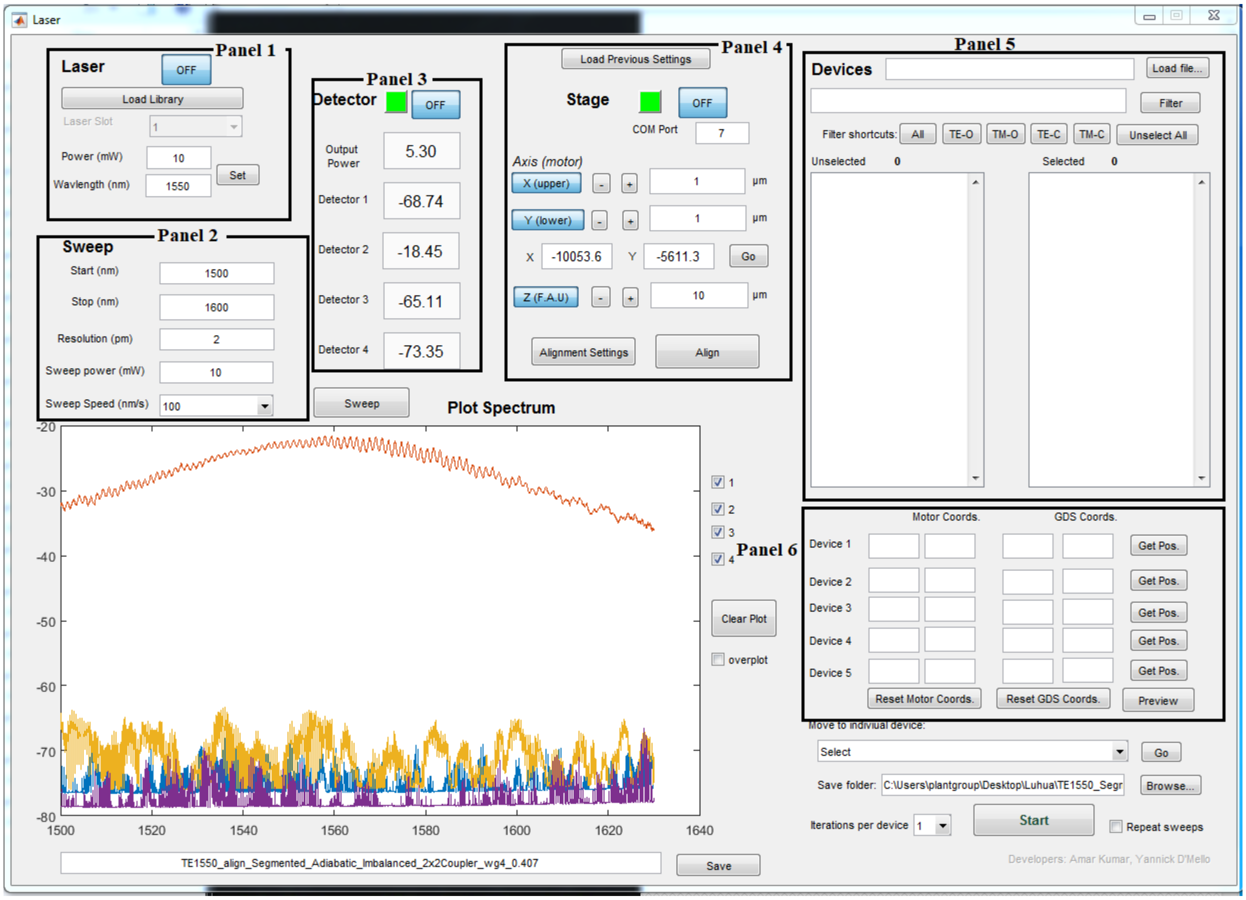

Fig. 2.3 GUI showing different control of PaNaMS.

port of the grating coupler to one of the ports of the detector, leaving three other ports empty. The trace (shown in red) in Fig. 2.3 is the spectral response obtained while other traces (shown in purple, blue and yellow) are noise. It should be noted that even when the detector ports are left unconnected, low-level noises are detected. However, the power of these low-level noises is below -60 dB, which is insignificant for measurement. The spectral response at all four ports of the detector is significant when output from a device is expected at these ports. For example, in the case of a 1x4 splitter, which has one input and four outputs, all four traces are significant. The spectral Panel 5 area allows the user to load the devices' position on the GDSII file and select the devices that are to be measured. Different filters are applied to select an individual category of devices. In order to accurately generate an entire map of all the devices in GDSII files, the positions in these files need to be converted into motor coordinates (i.e., a coordinate system understood by the microprocessor in the motor-controller). For accurate mapping, multiple alignment grating couplers are placed on a single chip during design. Panel 6 in Fig. 2.3 requires the input position of any of these alignment markers. A minimum of three devices needs to be aligned manually, and their motor and GDSII coordinates are provided in this panel. In the same panel, the 'Get Pos.' option is used to automatically fill the motor coordinates when the device is manually aligned to the optimized position. The 'Preview' option shows the map of the position of alignment markers and the devices to be measured. Fig. 2.5 shows an example of one such map. Users are also allowed to move to specific devices by selecting the device name. The 'Save folder' option in Fig. 2.3 requires the path of the folder where all the measured data needs to be saved. The option 'Iteration per device' shows the number of times a specific device is scanned, with each scan starting from the same initial position. This option allows the user to test the repeatability of the device and the reliability of the measurement performed. The automated testing begins upon selecting the 'Start' button. Once testing is in progress, a pop-up window shows the current device being scanned and all the selected devices are tested consecutively. A progress bar, in the same pop-up window, shows the status of the remaining devices and the time left to complete the entire measurement.

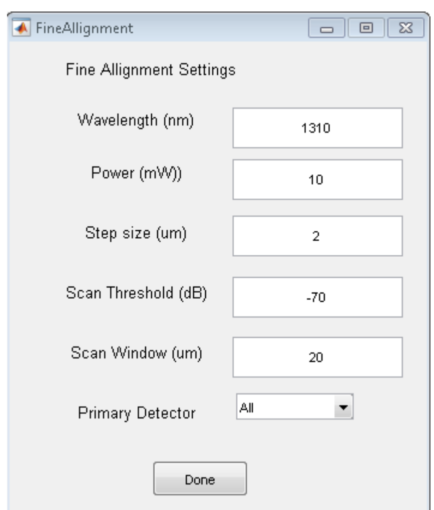

Fig. 2.4 The expanded window for the alignment setting present for fine alignment.

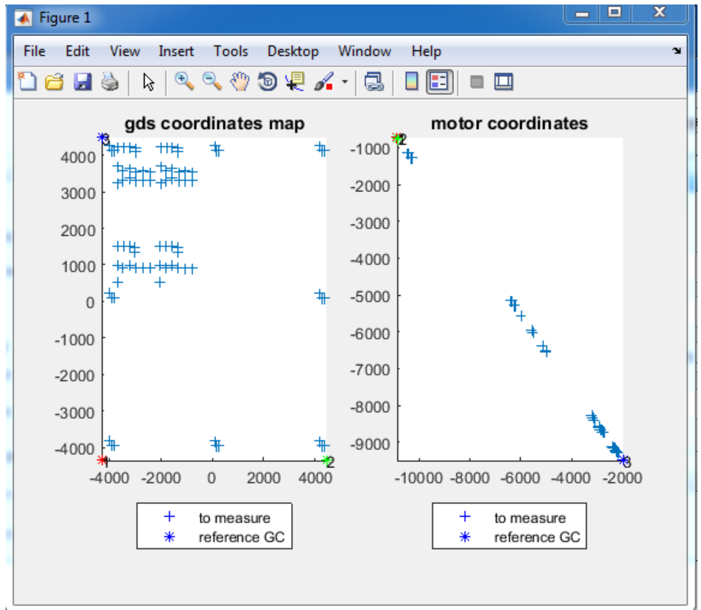

Fig. 2.5 The map showing alignment markers and devices to be measured in GDSII and motor coordinate systems.

2.3 Alignment Algorithm

PaNaMS uses a rapid optimization algorithm to perform an alignment. Initially, the system records a set of data points in both lateral and longitudinal dimensions during a rough scan based on the window size and scan steps provided by the user in the window as shown in Fig 2.4. Assuming the expected trend for the recorded data-points to follow is a 2-D Gaussian, the algorithm is designed to perform the interpolation. Interpolations are done to find the centroid of the shape obtained, as this centroid will be the optimum position of the device being tested. Once the algorithm identifies an optimum position, the search becomes finer, and another set of data points in the finer area is scanned to ensure the position predicted by the algorithm is optimized. The search stops if the value of power detected is consistent within a limit of 3 σ (σ being the standard deviation of the current Gaussian). At this point, it is assumed that search convergence is reached. If the algorithm did not find an optimized position with the first scan, the mesh size of the scanning area increases. The search for an optimized position is now in a larger area, and the same procedure is followed to find a value within 3 σ. Fig. 2.6 shows the results graphically after performing different iterations to obtain an optimized position.

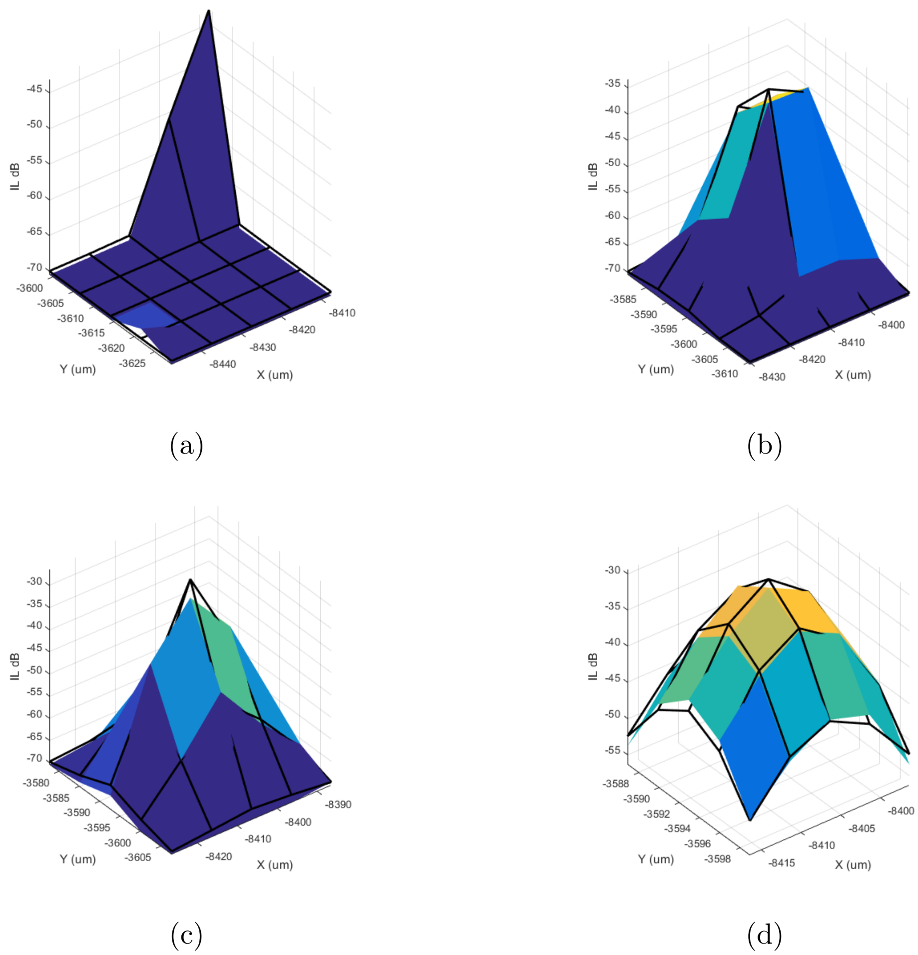

Fig. 2.6 Results from different stages when 2-D Gaussian interpolation is performed: (a) initial results obtained from the first scan; (b) performing second interpolation near the peak to see if a better IL can be achieved; (c) when the peak power has improved to be around -35 dB a finer search is performed; and (d) final results after convergence has reached within the limit of 3σ.

2.3.1 Implementation

PaNaMS gives the users complete flexibility while carrying out measurements on passive devices. The system can carry out an automated measurement on a single port device to multi-port (up to 4 ports) devices. The user can perform individual sweeps at their desired power and wavelength depending upon the laser. For multi-port devices like MMI, the user may be required to align the device based on outputs from all ports. The optimization algorithm is also adaptive to the best position, which can be achieved based on results from a single or all the output ports. The ability to do accurate coordinate transformation is one of the core functionalities of PaNaMS. In order to carry out an automated measurement, the user must orient the chip using alignment markers (i.e., with at least three of the devices manually). This alignment allows the system to generate a mapping between the motor coordinates and the gds coordinates. Motor and gds coordinates include the position of the devices as per feedback from the encoder and according to GDSII files, respectively.

2.4 Future Work

Although PaNaMS can perform the task accurately, upgrades to this system can be proposed. The GUI can be updated to include feedback from the cameras. This update will avoid the hassle of switching the windows of the camera and the GUI. The manual step of orienting the chip with the alignment markers is time-consuming. The user must also put extra effort into recording motor coordinates and the coordinates in the GDSII files. These steps of manual alignment can be upgraded using the technique of machine learning and computer vision. The techniques would involve placing the chip on the stage and performing rough scans to find the alignment markers. Once the alignment markers are located, optimized positions can be obtained using alignment algorithms. Since there is feedback coming from the camera, simple edge detection can be performed to find the corners of the chip, which will enable faster alignment to the reference devices. In addition, a fully automated active stage where probes can be landed on the chip using the feedback from the camera will be beneficial in carrying out measurements.

Chapter 3

Subwavelength Grating Couplers

This chapter discusses the working principle of grating couplers and the subwavelength structures. Section 3.1 introduces the grating couplers. Section 3.2 details the working of a grating coupler, and section 3.3 talks about the subwavelength structures. Section 3.5 mentions various simulation parameters and design techniques, and lastly, sections 3.6 and 3.7 elucidate the results obtained after fabrication, and the future work prospects, respectively.

3.1 Introduction

The efficient coupling of light into the chip is the primary step for a SiP device to work. Here, it is assumed there is no direct light source present on the chip (having a light source on the chip is an active research area in itself [14]). So, the light from an external source (primarily laser) is coupled into the circuit. This thesis explores the use of diffraction grating couplers for efficient coupling. As a result of the significant difference in the refractive index of silicon (serving as waveguide core), and silica or air (serving as cladding (see Table 3.1)), several modes of propagation can be confined into the waveguide. This difference has also helped in achieving nano-scaled photonic devices and integrating them with other CMOS technologies [15]. The downside of the same is that there is a substantial modal mismatch between the modal area of a single-mode fiber (SMF) and that of silicon photonic single-mode waveguide, which gives rise to a large number of practical limitations and losses.

Table 3.1 Refractive index of silicon (Si) and silica (SiO_2) [16, 17].

Wavelength	Material	Refractive Index
1310 nm	Si	3.4694
	SiO_2	1.4468
1550 nm	Si	3.4467
	SiO_2	1.4440

3.1.1 Various methods of coupling light into the waveguide

Any method that couples light from fiber into the chip uses the mechanism of spot-size conversion from fiber to chip or vice versa. However, this step involves a significant loss in intensity of the input light [18, 19]. Some of the popular techniques of coupling include - prism coupling, grating coupling, butt coupling and end-fire coupling. Prism and grating coupling use a prism and grating coupler, respectively, as an instrument to convert the input beam of light into a spot size that is the same as that of the waveguide. In this case, light is launched at a specific angle such that the propagation constant of a particular mode inside the waveguide is phase-matched with the input beam. However, prism coupling is not a widely-used mechanism due to its practical limitations, as it requires the material of the prism to have a refractive index greater than silicon. Besides, prism coupling can also damage the surface of a waveguide unless it is a planar waveguide. Butt coupling and end-fire coupling involve launching light directly from the fiber into the waveguide. While butt coupling involves directly launching light from the fiber to the waveguide, end-fire coupling uses a lens to focus the beam. A symbolic representation of these methods of coupling is shown in Fig. 3.1 [20].

3.2 Working Principle

Waveguides in photonics are analogous to the electrical wires, and while the former guides photons, the latter guides electrons. The entire principle of propagation works based on total internal reflection (TIR) because of the significant difference in refractive index between core and cladding. Fig. 3.2 shows a typical schematic of different types of waveguides - (a) slab waveguide, where light propagates through a slab of silicon mounted on a buried oxide (here, the outer cladding can be air or an oxide, like SiO_2, with a similar refractive

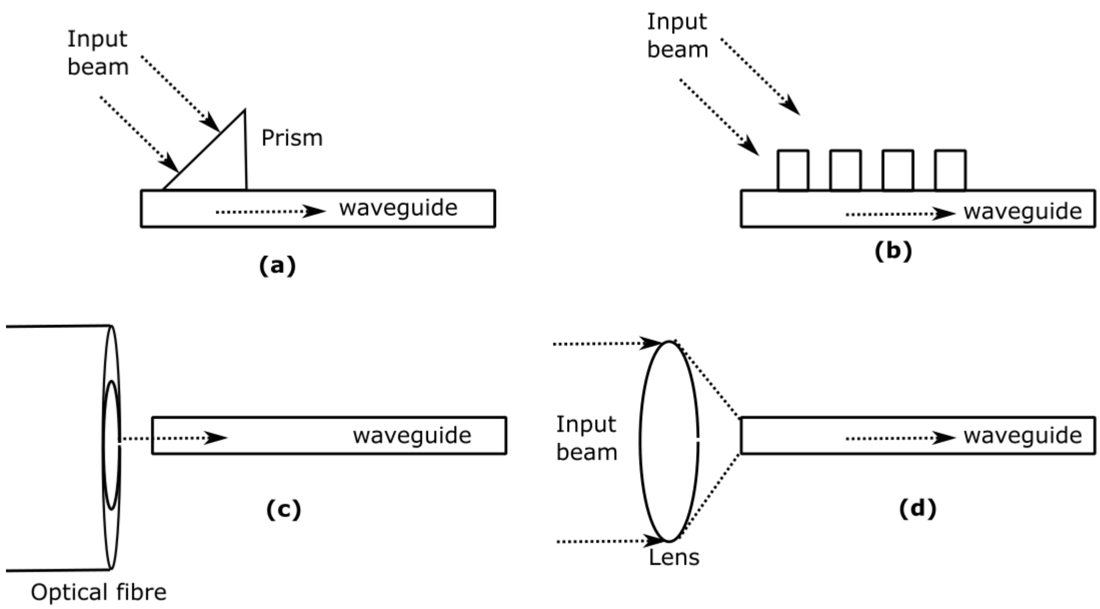

Fig. 3.1 A schematic of different types of coupling: (a) prism coupling, (b) grating coupling, (c) butt coupling, and (d) end-fire coupling. The picture is reproduced from [20].

index); (b) channel waveguide, where the propagation is carried only on a channel or strip mounted on the buried oxide surrounded by a media with a low refractive index; and (c) ridge waveguide, which is similar to channel waveguide with the only difference being in the height of the silicon. In this case, silicon is at different heights with a step-like formation and is surrounded by oxides. The mechanism of coupling light into the waveguide includes a phase-matching condition. In other words, the propagation constant of light in medium 1 in the z-direction is the same as the propagation constant in medium 2 (Fig. 3.3). Therefore, the z-direction propagation constant in medium 1 will be given by Eq. (3.1) where k_0 is the propagation constant in free space and n_1, n_2 and n_3 are refractive indices of medium 1, 2 and 3, respectively. Furthermore, the phase-matching condition will be given by Eq. (3.2), where p is the waveguide propagation constant.

$$k_z = k_0 n_1 sin(a) \tag{3.1}$$

$$p = k_z = k_0 n_1 sin(a) \tag{3.2}$$

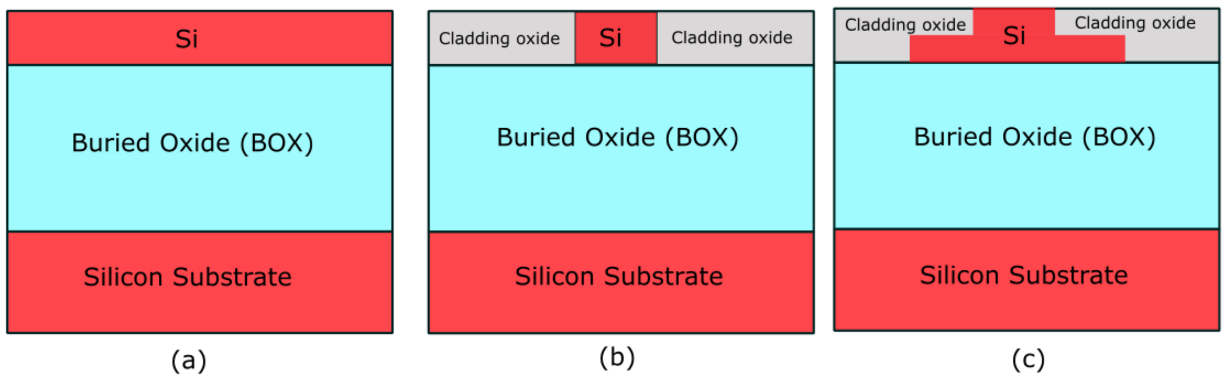

Fig. 3.2 A schematic front view of different types of waveguides: (a) slab waveguide, (b) channel waveguide, and (c) ridge waveguide.

A grating has periodic structures of silicon, which modulates the refractive index so the phase-matching condition can be met. The modulated propagation constant, β_m, when the grating is not present, is given by Eq. (3.3), where β_w is the propagation constant of the optical mode, Λ is the grating period and $m = \pm 1, \pm 2, \pm 3$, etc.

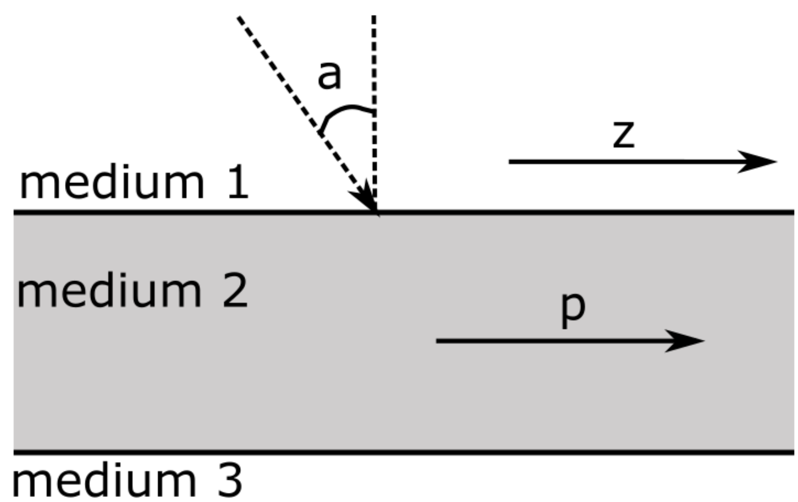

Fig. 3.3 Coupling light from free-space into the waveguide.

$$\beta_m = \beta_w + \frac{2m\pi}{\Lambda} \tag{3.3}$$

As a result of the relation developed from Eq. (3.2), only negative values of m are acceptable in Eq. (3.3) for having a phase-matching condition. Other diffraction orders of a value of m higher than 1 can be suppressed during the design phase; hence, only $m = -1$ is used. After combining with Eq. (3.2), the Eq. (3.3) therefore transforms into Eq. (3.4).

$$\beta_w - \frac{2\pi}{\Lambda} = k_0 n_1 sin(a) \tag{3.4}$$

Expressing β_w in terms of an effective refractive index, n_{eff}, Eq. (3.4) is written as Eq. (3.5)

$$k_0 n_{eff} - \frac{2\pi}{\Lambda} = k_0 n_1 sin(a) \tag{3.5}$$

Finally, substituting k_0 and placing $n_1 = 1$(air), the period of gratings is calculated as in Eq. (3.6).

$$\Lambda = \frac{\lambda}{n_{eff} - sin(a)} \tag{3.6}$$

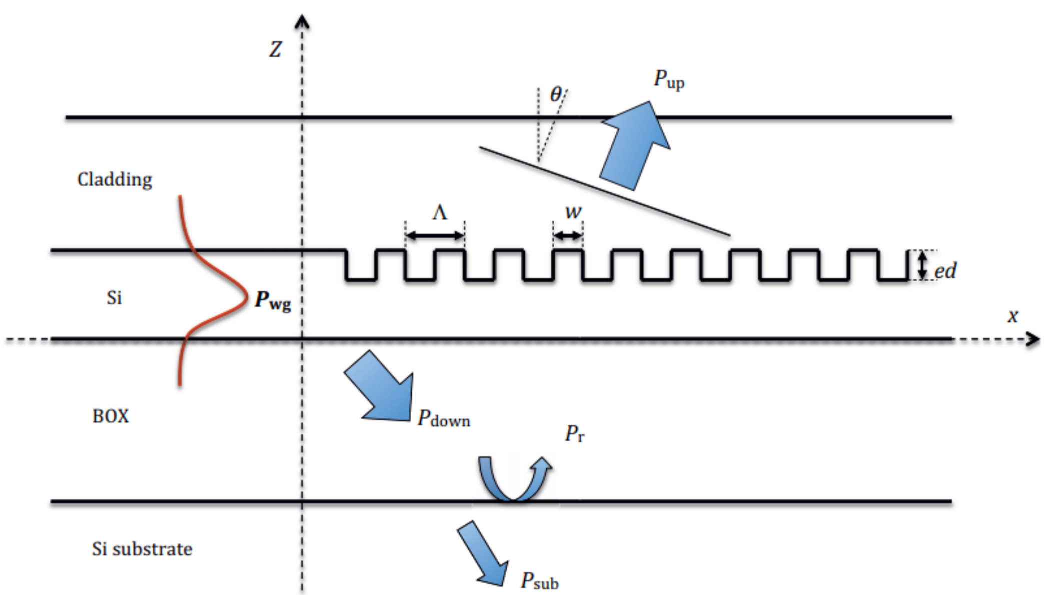

Fig. 3.4 Complete schematic of a grating coupler. The picture is taken from [21].

Fig. 3.4 shows the complete schematic of a grating coupler. Various design parameters in Fig. 3.4 can be described as follows:

- The coupler has an outer cladding (generally air or an oxide), a core (Si), and a bottom cladding (buried oxide (BOX)) for making the waveguide, while the effective refractive index of the slab waveguide is n_{eff};

- Λ is the grating period (i.e., the length at which the Si periodic pattern repeats itself);
- W is the width of each Si grating in a period;
- ff is the fill factor, which shows what fraction of a period Λ is filled with Si and can be represented as $ff = W/\Lambda$;
- ed denotes the etch depth of Si, while from the fabrication point of view, the etch depth for devices is 220 nm;
- θ is the incident angle of the grating coupler;
- P_{wg}, P_{up}, P_{down}, P_{sub} and P_r denote the power coupled in the waveguide, diffracted in the upwards region of the waveguide, diffracted in the downward region of the waveguide, coupled in the substrate and reflected from the substrate, respectively.

Some of the key characteristics used to quantify and evaluate the performance of a grating coupler are:

1. *Directionality:* the ratio between the power diffracted upwards (P_{up}) and the input power from the waveguide (P_{wg}), which is expressed in decibels (dB) as $10log_{10}.(P_{up}/P_{wg})$.
2. *Insertion loss:* the ratio between the power coupled into the fundamental mode of the fiber (P_{fiber}) and the input power from the waveguide (P_{wg}), which is usually expressed in decibels (dB). Insertion loss can be expressed as $10log_{10}.(P_{fiber}/P_{wg})$. It is also sometimes referred to as the coupling efficiency.
3. *Penetration loss:* the ratio between the power lost in the substrate (P_{sub}) and the input power from the waveguide, which is $10log_{10}.(P_{down}/P_{wg})$.
4. *Back-reflection:* Since there is a difference between the refractive index of BOX (lower refractive index) and Si substrate (higher refractive index), some part of the P_{sub} is reflected in the core. The ratio between the reflected power and the input power from the waveguide is called the back reflection to the waveguide, or optical return loss, and is usually expressed as $10log_{10}.(P_{back-wg}/P_{wg})$. This back-reflection will create

Fabry-Perot oscillations by reflecting back and forth between the input and output grating couplers [22, 23].

5. *Bandwidth:* This is usually defined by 1 dB or 3 dB bandwidth, which determines the wavelength range over which the insertion loss is 1 dB or 3 dB lower than the peak coupling efficiency, respectively.

3.3 Subwavelength Structures

Subwavelength structures have their physical dimensions comparatively smaller than the wavelength of operation. These structures allow finer control over the refractive index of material by adjusting the arrangement of materials in space. Besides, these periodic structures prevent diffraction and behave like a homogeneous medium given that the periodicity does not satisfy the Bragg condition for coupling light into other confined or radiative modes [24, 25].
Fig. 3.5 shows a subwavelength structure with varying periods Λ_1 and Λ_2, where a and b are structures of two different thicknesses, followed by alternating layers of different refractive indices.

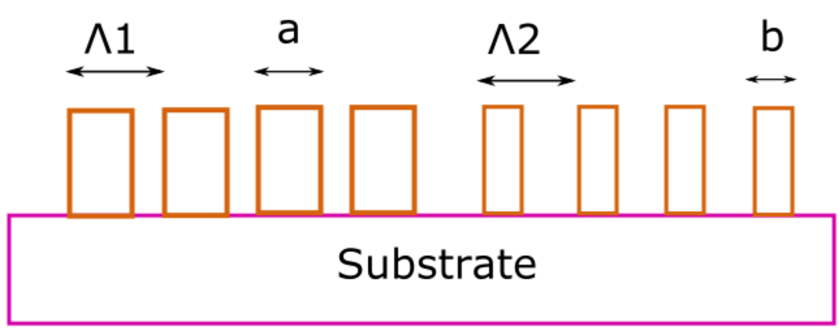

Fig. 3.5 A simple subwavelength structure. The different colored sections have different refractive indices.

The properties of this periodic waveguide are related to the free-space wavelength. Fig. 3.6 shows a schematic $k - \omega$ diagram of the periodic waveguide. As shown in Fig. 3.6, and depending upon the frequency, the periodic structure can operate in a subwavelength regime, Bragg-reflection regime or radiation regime. As can be seen in Fig. 3.6(a), that propagation constant (k_B) increases with an increase in the ω such that $\omega < \omega_1$ and the subwavelength structure acts as a normal waveguide. In the frequency range corresponding

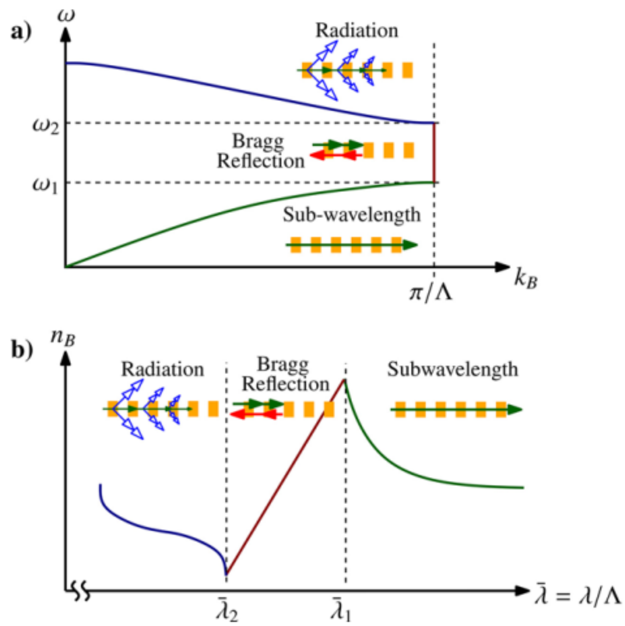

Fig. 3.6 (a) Schematic dispersion diagram in the first Brillouin zone of a periodic waveguide with lengthwise propagation (along the z-axis), (b) an equivalent representation of the Bloch mode effective index (n_B) of the periodic waveguide as a function of the wavelength-to-pitch ratio inline image. Higher order diffraction and reflection bands are not shown. The figure is taken from [26].

to the photonic gap, Bragg reflection occurs and light cannot propagate. Additionally, the propagation constant is $k_B = \pi/\Lambda$. Above this frequency, the Bloch modes are leaky and propagate out of the waveguide. The electric fields observed in all these cases can be seen in Fig. 3.7. These structures find broad application in almost every sensing application ranging from bio-sensors to calibration filters [27, 28, 29], anti-reflective coatings on bulk optical surfaces [30], planar mirrors [31], anti-reflective gradient-index structures and interference mirrors [32, 33], and crossings [34].

3.4 Literature Review

The IL depends upon the thickness of the top silicon layer and the BOX because these two determine the effective refractive index as well as the phase-matching conditions of different wavelengths at the interface between the grating layer and the buried oxide layer. Chen et al. [35] obtain a coupling loss of 1.2 dB at 1530 nm with the design of 340 nm Si and

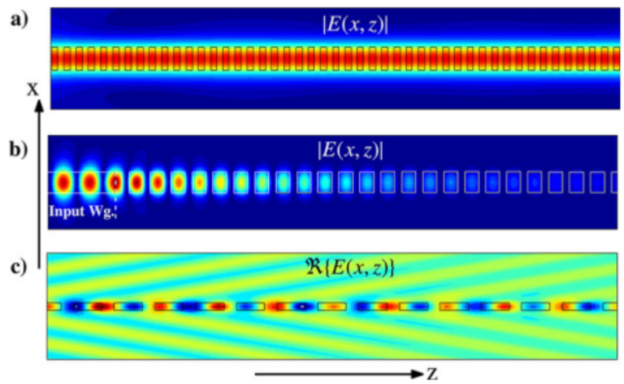

Fig. 3.7 Propagation in a periodic structure waveguide: (a)Sub-wavelength Regime: the structure behaves like a normal waveguide; (b) Bragg Reflection Regime: the propagated light gradually attenuates; and (c) Radiation regime: propagated light is radiated out of the waveguide(only $\kappa = -1$ diffraction order is shown in the image). The figure is taken from [26].

2 μm BOX following shallow etches for the fabrication process. Yi Zhang et al. [36] use a grating coupler with an insertion loss of 4.4 dB with a peak near the 1545 nm wavelength and a 1.5 dB bandwidth of 45 nm. They use a standard 220 nm shallow etch Si and 2 μm BOX. Roelkens [37] et al. use a grating coupler at a wavelength of 1530 nm with 1 dB optical bandwidth of 50 nm. The device is on a standard 220 nm Si with 2 μm buried oxide of silica.

Distributed Bragg reflectors at the bottom and top overlays are used to reduce the insertion loss. Taillaert et al. [38] use a grating with a footprint of 13 μm long and 12 μm wide with a two pair bottom reflector. They obtain a coupling loss below 1 dB over a wavelength range of 35 nm for TE polarization. Zhang et al. [39] use a silicon nitride platform with bottom mirrors to improve the coupling efficiency at 1490 nm. They obtain a peak coupling efficiency of -2.5 dB and 1 dB bandwidth of 53 nm. Vermeulen et al. [40] use a silicon overlay on a 200 mm wafer in a CMOS pilot line and obtain a coupling efficiency of -1.6 dB and a 3 dB bandwidth of 80 nm. The issue with using a bottom mirror or overlay is that they require a customized process and use non-standard wafers.

There is also a significant amount of research conducted in designing the subwavelength grating structures. Mateus et al. [41] use subwavelength grating with a broad reflection spectrum ($\Delta\lambda/\lambda > 15\%$) and high reflectivity ($R > 99\%$). They also propose that similar performances are achievable on a silicon platform as well as $GaAs - Al_2O_3$, GaN-air or

$ZnSe - CaF_2$. Halir and Cheben et al. [42] use the SOI platform to demonstrate a grating coupler with a single etch step and a coupling efficiency of 3.7 dB. The device has a 3 dB bandwidth of 60 nm and a minimum feature size of 100 nm, which allows it to be manufactured easily by DUV lithography. Kang et al. [43] use a focusing subwavelength for efficient coupling of mid-infrared light into suspended Ge photonic integrated circuits. The device has a maximum coupling efficiency of -11 dB with 1 dB bandwidth of 58 nm at a central wavelength of 2370 nm. Apodizing the subwavelength structure on the SOI platform is proposed by Benedikovic [44], which helps to achieve high efficiency with a single etch-step. They obtain a peak coupling efficiency of -2.16 dB at the central wavelength of 1550 nm.
In this work, I propose the use of an etched structure in the tapered region to further improve the performance of a subwavelength grating coupler proposed by Wang et al. [45]. The selection of this grating coupler is based on the fabrication facility accessible to me.

3.5 Simulations

The aim is to design a low loss subwavelength grating coupler. The simulation and fabrication were carried out for grating couplers with TE polarization. The design was carried out in four major steps:

1. A theoretical expression for 1 dB bandwidth of the grating coupler that depends on the group refractive index and the fiber incident angle used. Eq. (3.7) provides the phase-matching condition [46] for the grating diffraction in a grating coupler.

$$\kappa_0.n_{eff} = \kappa_0.n_c.sin(\theta) + m.\frac{2\pi}{\Lambda} \tag{3.7}$$

   where, $\kappa_0 = \frac{2\pi}{\lambda}$, n_{eff} is the effective refractive index of the gratings, n_c is the refractive index of the cladding, θ is the angle of incidence in free space, Λ is the grating period, and m is the diffraction order (here, m=1). Eq. (3.8) provides the relationship between the actual wavelength and the diffraction angle.

$$\frac{n_{eff}(\lambda)}{\lambda} = \frac{n_c sin(\theta)}{\lambda} + \frac{1}{\Lambda} \tag{3.8}$$

   Eq. (3.9) provides the expression for the bandwidth of a grating coupler which is approximately derived by a derivative of $\lambda(\theta)$ [46, 45].

$$\Delta\lambda_{1dB} = \Delta\theta_{1dB}.2\left|\frac{d\lambda}{d\theta}\right| = \Delta\theta_{1dB}.2\left|\frac{-n_c.cos(\theta)}{\frac{1}{\Lambda} - \frac{dn_{eff}}{d\lambda}}\right| \tag{3.9}$$

where, $\Delta\theta_{1dB}$ is a constant dependent on the fiber properties. Simplifying the expression in Eq. (3.9) and the expression for group index in Eq. (3.10) results in a compact expression for the 1 dB bandwidth of the grating coupler provided in Eq. (3.11).

$$n_g = n_{eff} - \lambda\frac{dn_eff}{d\lambda} \tag{3.10}$$

$$\Delta\lambda_{1dB} = \Delta\theta_{1dB}.2\left|\frac{-n_c.cos(\theta).\lambda}{n_g - n_c.sin(\theta)}\right| \tag{3.11}$$

Since $\Delta\lambda_{1dB}$ and n_c are constants, bandwidth will only depend upon the group index and the incident angle for a fixed value of λ. From Eq. (3.11), it is clear that a broader bandwidth can be achieved by reducing the group index of the grating or increasing the incident angle. The optimal incident angle is a function of the group index of the grating. The simulated n_g for an unetched silicon waveguide is approximately 4.2, and the simulated n_g for a one-dimensional subwavelength grating with an overall fill factor of 0.2 is approximately 2.2 [45]. From this expression, an angle of 25° is chosen, which is the optimal incident angle for an n_g near the center of n_g, ranging from 2.2 to 4.2.

2. Based on this expression, a specific incident angle (i.e., the angle at which light will be launched into the grating coupler) is chosen for design optimization.

3. A commercial software, Lumerical [47], is used to perform all the simulations. The 2-D FDTD simulation is carried out to have an idea of the performance of the device design. The optimization involves sweeping all the geometrical parameters (i.e., λ, p, Λ, l, L and Hl) shown in Fig. 3.9. Sweeping these parameters in the range of their expected values requires creating different models. Each model has a specific set of values for the above-mentioned geometrical parameters. Hence, to have faster optimization, a 2-D FDTD was used. Differences and deviation from actual behavior are expected if a 2.5 varFDTD or a 3-D FDTD simulation is performed. A complete analysis of the difference in speed and accuracy during simulations among the 2-D

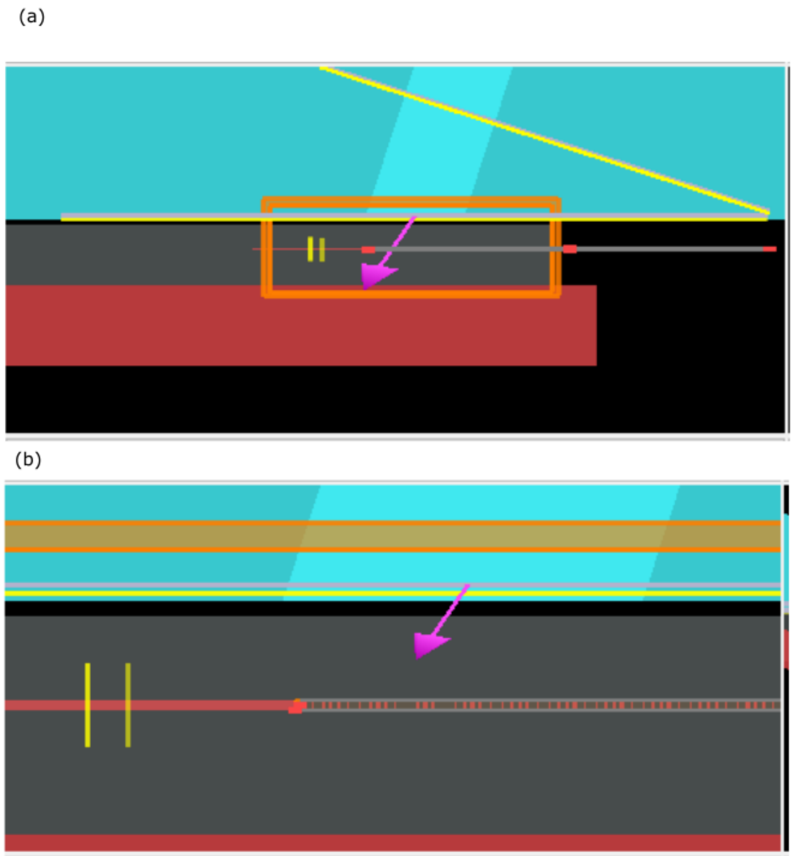

Fig. 3.8 The FDTD simulation of the GC without any etching in the taper region: (a) simulation boundaries and (b) a closer look at the design parameters.

FDTD, 2.5 varFDTD and 3-D FDTD can be found on Lumerical's webpage [48, 49]. A detailed analysis of the performance of a grating coupler simulated under the 2-D and 3-D FDTD is also found in [50, 45]. Comparing the speeds, the 2-D FDTD is faster in this case without compromising significantly on the calculation efficiency. Approximately 1200 simulation files were executed to arrive at the optimized values mentioned in section 3.6. Hence, a complete 3-D FDTD or 2.5 varFDTD simulation will take a long time in optimization; thus, the 2-D FDTD was chosen. Finally, when properly optimized values were obtained, a complete 3-D FDTD simulation was carried out to validate the result.

The FDTD method uses the brute force calculation of Maxwell's equations for every mesh point within the given time domain. The simulation stops if the specified

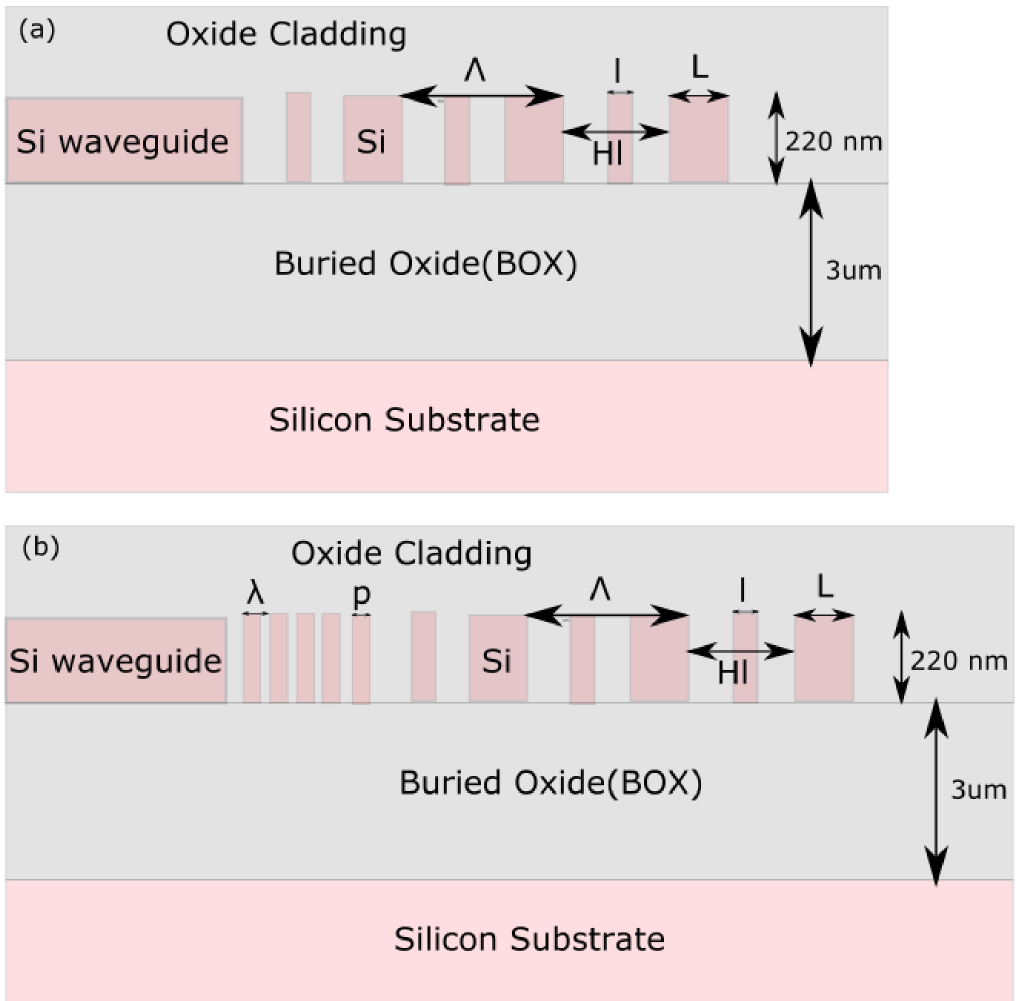

Fig. 3.9 Side view of the designs of the SWGC: (a) exact design mentioned in [45], and (b) a new subwavelength region introduced with period λ and width, p.

error convergence is reached before the maximum allotted time. While the main advantage of using this technique of calculation is that any arbitrary shape can be easily simulated, its drawback lies in the fact that it cannot be used for long structures as the time for convergence will be too large. Additionally, results are sometimes affected by the grid size if the feature sizes are too small. Since the footprint of grating couplers is small, the 2D-FDTD is ideal for simulation.

A schematic of the simulation boundaries is shown in Fig. 3.8. The orange region in Fig. 3.8 shows the simulation boundary, and I have used the perfectly matched layer (PML) periphery condition so any radiation at the boundary will propagate out of the computation area and not interfere with the fields inside to cause any reflections. The yellow lines in Fig. 3.8 show the frequency domain power monitors and are used to record the power flow information in the specified location. The light blue area shown in Fig. 3.8 represents the fiber with a specified launch angle, and the pink arrow shows the source of light with the head of the arrow pointing in the direction in which light will propagate.

4. Various parameters defining the subwavelength structure are optimized using PSO (see Sec. 4.4) for obtaining the maximum efficiency. Fig. 3.9 shows the side view of the designed grating coupler expected to have a low back reflection. The central wavelength of interest is 1570 nm, and the waveguide geometry chosen is 450 nm (width) x 220 nm (height). The Λ is the period of the high and low refractive index region, l is the width of the thinner region and L is the width of the thicker region. The standard 220 nm etching process is used for the height of Si, and the thickness of the BOX is 3 μm. The new proposed structure with a subwavelength structure is shown in Fig. 3.9(b) and the periodic structure has a period, λ, and width, p.

3.6 Results and Discussion

The subwavelength grating coupler is designed on the SOI platform with 220 nm silicon and 3 μm buried oxide. The gratings consist of alternate regions of high and low refractive indices. The region of low refractive index is created by etching away silicon. Fill factor, ff, is the quantity that represents the fraction of the region filled with silicon in a period Λ. The fill factors of the low and high refractive index regions, denoted as ff_l and ff_H, will be given by $N_l * l/\Lambda_l$ and $N_H * L/\Lambda_H$, respectively, where λ_l and Λ_H are periods of thinner and thicker width regions. The optimized value of Λ and ff are 1130 nm and 0.5, respectively. The optimized values of ff_l and ff_H are 0.13 and 0.49, respectively. The optimized values of the number of thinner (N_l) and thicker (N_H) width regions obtained after PSO are 3 and 2, respectively. The λ is the period of the subwavelength structure, while p is the thickness. The optimized value of λ and p are 280 nm and 121.8 nm, respectively. This subwavelength structure in the tapered region provides a simulated transmission of about 97% in the given wavelength spectrum. So, the design is also compatible with the manufacturing process, as the minimum feature size is greater than 100 nm. The GDSII layout of the two types of grating coupler is shown in Fig. 3.10 with sub-image (a) showing the subwavelength grating coupler without any etching in the taper, while the grating coupler with etching in the tapered region is shown in sub-image (b). Lastly, θ is the value at which light from the fiber is launched into the grating coupler. Table 3.2 shows the optimized values of all the design parameters.

Table 3.2 Optimized value of different design parameters

Sl. No.	Parameter	Value
1	θ	25°
2	Λ	1130 nm
3	ff	0.5
4	ff_H - ff_l	0.49 - 0.13
5	N_H - N_l	3 - 2
6	λ - p	280 nm - 121.8 nm

A back-to-back grating coupler forms a Fabry Perot cavity, and when a measurement is carried out, there are slight ripples in the response obtained, which lead to additional noise. In order to have a design of an SWGC with low back reflection, the work mentioned in [45, 51] is reproduced and then extrapolated further to etch the tapered part of the GC as well. The simulated transmission and reflection spectra of the optimized grating couplers are shown in Fig. 3.11. As compared to the grating coupler with no etch in the tapered region, the one with etching has lower back reflections. The values of the maximum and minimum back reflections in the case of the grating coupler with no etching are -12.9 dB

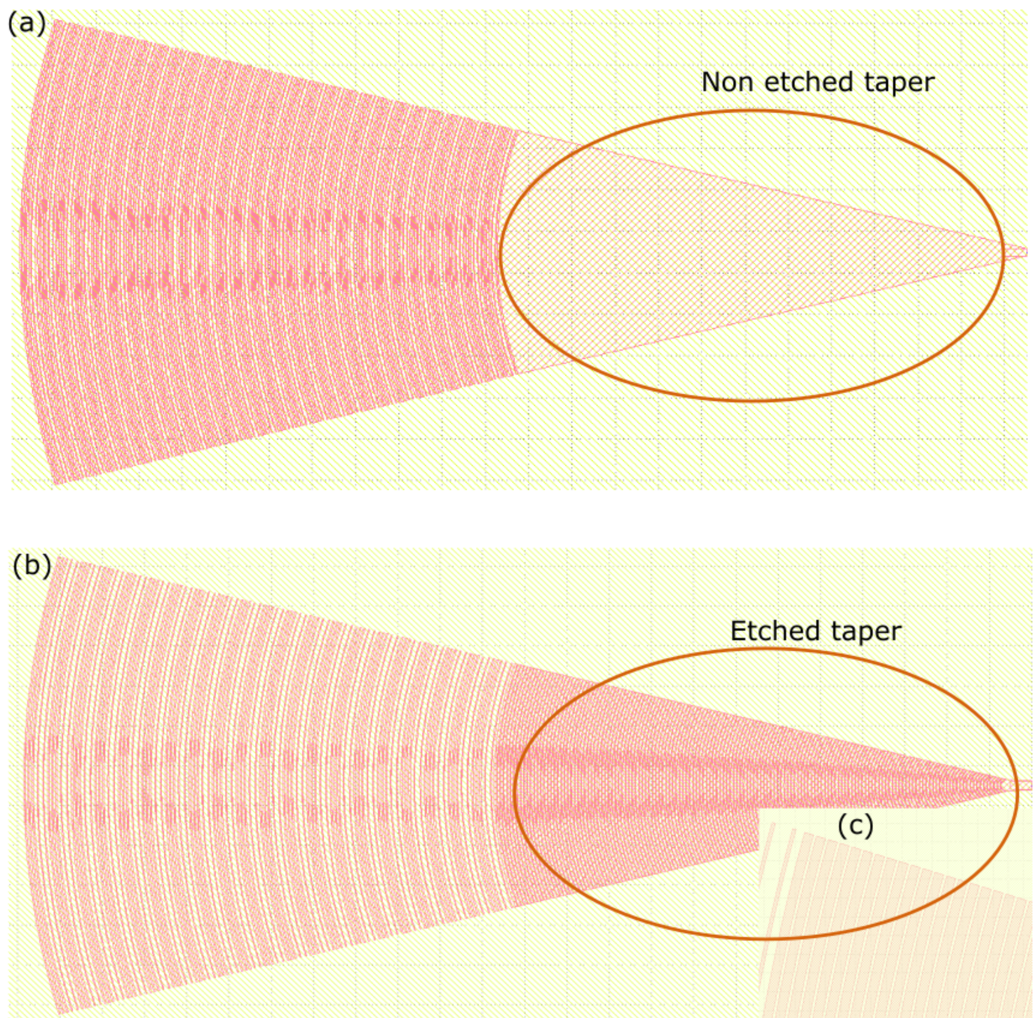

Fig. 3.10 A comparison of the GDSII of the two designs of GC: (a) the tapered region is not etched, (b) the tapered region is etched, and (c) the inset shows the etched area.

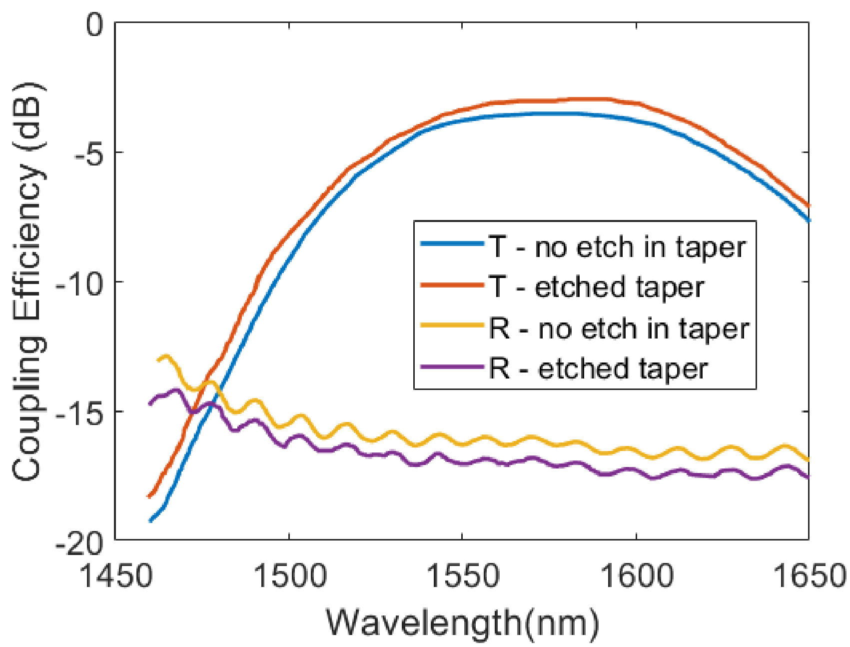

Fig. 3.11 The comparison of simulations of CE in two different designs (T: Transmission and R: Reflection).

and -16.9 dB, respectively. The values in another case with a tapered etch are -14.2 dB and -17.6 dB. This improvement could be a result of the reduction in the cavity formed between a grating coupler pair. In addition, the coupling efficiency is also improved from -3.65 dB to -3 dB due to the slight change in the design structure. The figure of merit used for optimization was defined as the product of 1 dB bandwidth and the CE. Here, CE is defined as $10log_{10}(P_{wg}/P_{in})$, where P_{in} is the input power coupled into the input grating coupler and P_{wg} is the power coupled from the output grating coupler to the waveguide. There is also an improvement in the 1 dB bandwidth of the grating coupler from 88 nm to 94 nm with a central wavelength of 1578 nm. Fig. 3.11 compares the CE of the two designs: one without etching in the tapered region and the other with a subwavelength structure in the tapered region. Therefore, in all aspects (i.e., CE, back-reflection and 1 dB bandwidth) the grating coupler with etch in the tapered region performs better. In order to fulfil the experimental requirement, a fiber with a polish angle of 25.3° was used, and the incident angle was adjusted to meet the specific requirement of 25°. Fig. 3.12 compares the measurement results of the two different designs. It should also be noted that measurements are performed on back-to-back grating couplers (i.e., a pair of grating

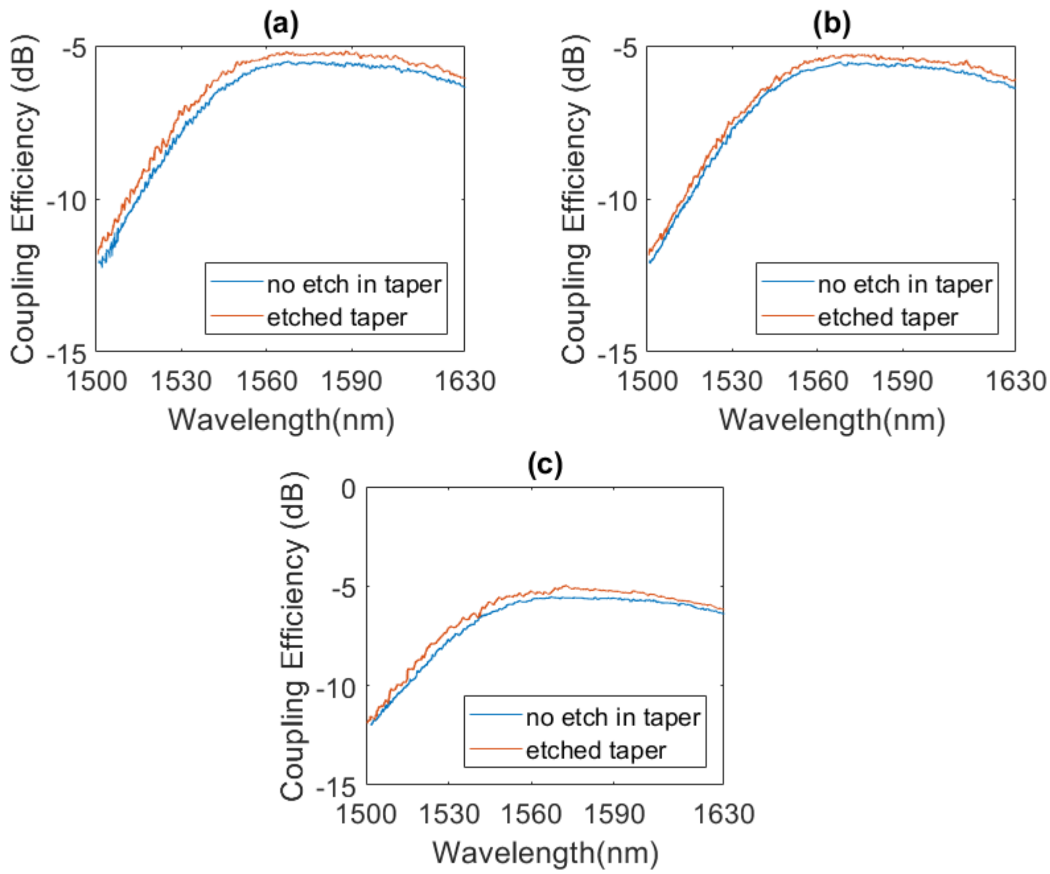

Fig. 3.12 The comparison of measurements of CE in two different designs (the CE is adjusted to show the result for a single grating coupler): (a) case 1, (b) case 2, and (c) case 3.

couplers). While showing the measurement results of one grating coupler, it is assumed that both the couplers are identical in performance.

Three similar designs of the grating coupler were fabricated and tested to discover if the design was repeatable. Fig. 3.12 shows the measurement results. In all three cases, the grating coupler with etching in the tapered region performs better than the one without any etch. The improvement in performance is because of the increase in coupling efficiency and 1 dB bandwidth. From Fig. 3.12, the coupling efficiency of the grating coupler with etch in the taper is higher than the coupling efficiency of the grating coupler without taper throughout the wavelength range of 1500 nm - 1630 nm. Table 3.3 summarizes the measurement results in all three repeatable cases of the grating couplers. From the

Table 3.3 Measurement results of the grating couplers

	Feature	GC without etch in taper	GC with etch in taper
Case 1	CE	-5.51 dB	-5.17 dB
	1 dB bandwidth	88 nm	93 nm
Case 2	CE	-5.53 dB	-5.29 dB
	1 dB bandwidth	88 nm	91 nm
Case 3	CE	-5.53 dB	-4.95 dB
	1 dB bandwidth	87 nm	93 nm

table, it can be inferred that the devices in all three cases show similar behavior. The best performing grating coupler is the one mentioned in case 3 with a coupling efficiency of -4.95 dB and a 1 dB bandwidth of 93 nm. This improvement in back reflection might come from the fact that the Fabry-Perot cavity formed between the two back-to-back grating couplers are reduced, which then reduces the space available for oscillations. Due to this reduced back reflection, there is an improvement in the insertion loss of -0.34 dB, -0.24 dB, and -0.58 dB in three cases with the same structure of the grating coupler.

3.7 Future Work

A large section of subwavelength structures remains unexplored, which could lead to the discovery of efficient devices in terms of insertion loss or bandwidth. Optimizing the geometry of the etched section can also lead to devices with a smaller footprint. The next big leap will be the development of a polarization-independent grating coupler, which is challenging to design because of the requirement of effective refractive indices for the TE and TM modes. Further effort can be made to design chirped grating with sub-wavelength structures to have lower losses. New designs, such as sub-wavelength structures with slanted gratings, can also help to suppress back reflections.

Chapter 4

Y-branch

This chapter provides a different approach to designing a Y-branch. Section 4.1 provides a simple introduction to the Y-branch and its properties. Section 4.2 discusses the working of a Y-branch, and section 4.3 provides a background to different research that has been carried out in this field. Section 4.4 discusses the optimization algorithm used for designing this Y-branch. Section 4.5 describes the simulation methodology and various geometrical parameters. Section 4.6 details the results collected after testing the fabricated device and how well they agree with the simulations. Finally, section 4.7 discusses the improvements using advanced algorithms for designing SiP passive devices. The work carried out in this chapter is a reproduction of the work presented by Zhang et al. [52] to design a 50-50 splitter in C-band.

4.1 Introduction

A Y-branch is one of the building blocks of the photonic circuit used for splitting and combining light [21]. Depending upon the requirements, a Y-branch can be used to split incoming light into N-ports (symmetrically or asymmetrically) and can combine input light from different ports into one single port or multiple ports. Fig. 4.1 shows a typical structure of the symmetrical Y-branch, which consists mainly of three different sections: an input port, a central region and an output port. The light enters the device from the input port, passes through the central region and finally comes out through the output ports. The geometry of the central region defines the behavior of the Y-branch. Symmetry in the central region of this device means that the intensity of light in the incoming port (the port on the left in Fig. 4.1) is split into two equal parts (received at the output ports in the right as in Fig. 4.1). The two branching outputs shown in Fig. 4.1 are in the shape of the cosine arc. They can also be in the shape of straight waveguides with a certain branching angle. However, an output branch with a cosine arc is more compact compared to the one with a straight waveguide. Apart from having the property of combining and splitting, the Y-branch also works as a multiplexer and a de-multiplexer [53, 54, 55, 56].

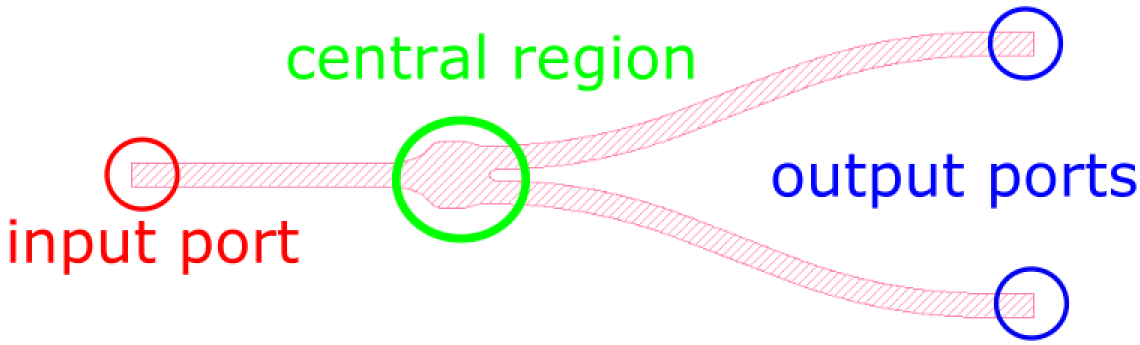

Fig. 4.1 A simple structure for a symmetric two port Y-branch.

4.2 Working Principle

The Y-branch acts as a splitter and a combiner depending upon the usage. For an input light with intensity, I, and electric field, E, coming through the input port, as shown in Fig. 4.1 when it goes through a 50/50 splitter Y-branch, the intensity at either of the output ports is $I/2$, and the electric field at either port is $E/\sqrt{(2)}$ as $I \propto |E|^2$. When the Y-branch acts as a combiner, the input light is split equally between the fundamental mode of the waveguide and the second-order mode. Thus, the light at the combined port will be $I/2$, and the electric field will be $E/\sqrt{(2)}$. Additionally, a Y-branch, when used as a combiner, cannot arbitrarily combine two incoherent lights.

4.3 Literature Review

A preliminary design of the Y-branch [54] is asymmetrical, where it acts as a multiplexer for the wavelengths of 660 nm pump and 1535 nm signal with coupling efficiencies of 85%

and 95%. Here, the performance of the Y-branch is determined by the coupling efficiency of the TE_{00} modes of the two signals: a pump and an input. The simple design and structure of this device make it easy to be manufactured in a single mask. Wang and Lu [57] use a multimode region before the splitting area of the Y-branch, and the shapes of the output bends are in the form of the cosine arc. They use a combination of a genetic algorithm and a gradient-based search method for geometric optimization of the device. Riesen and Love [58] and Driscoll et al. [59] also propose some asymmetric designs for the Y-branch to perform mode sorting. An asymmetric design enables the Y-branch to perform mode division multiplexing (MDM). Breaking symmetry between the upper and lower output ports of the Y-branch allows it to behave as a variable power splitter, as Shirafuji et al. [60] mention, where the power is controlled by adjusting the gap between the splits of the two output branches. Secondly, it behaves as wavelength multiplexers [61], a design that multiplexes and demultiplexes the 1300 nm and 1500 nm wavelengths using two asymmetric mode Y-branches, as well as mode-splitters in optical switches, as mentioned by Henry and Love [62].

These designs are further complicated by cascading different Y-branches to perform MDM and have a sizeable spectral bandwidth. Chen et al. [63] propose a 1 x N ($N \geq 4$) mode multiplexer based on a cascaded asymmetric Y-junction. The branches with a larger width supporting more modes are coupled with other branches having only the fundamental mode efficiently. For their design, they achieve a cross-talk of -21.8 dB with a bandwidth of 140 nm and an insertion loss of 0.03 dB. Garaot [64] proposes a slightly different design to perform mode sorting, where the device length is shortened using an adiabatic splitting between the branches. The mode conversion efficiency of their design is 0.98 with an insertion loss of 0.267 dB and 0.185 dB in the two output ports. Sometimes a theoretical design shows excellent performance, but the practicality of having the same performance within error limits is questionable because of sharp splits. There is an additional restriction to the minimum feature size that a foundry can fabricate. Hence, the technique of splitting light with equal intensity in both the branches with almost negligible loss is discussed in the following sections.

4.4 Optimization: PSO

Optimization is one of the significant steps in improving the design of SiP devices, as the geometry of different parts of the device depends on it. This chapter uses PSO as the optimizer for the design of the Y-branch. The PSO is an evolutionary algorithm based on the population dynamics of the particle and their behavior with the surrounding neighbors. Previously, evolutionary algorithms were based on the underlying principle of 'survival of the fittest' ([65, 66, 67]); however, PSO takes into account the social behavior of each particle and velocity attached to it ([68, 69, 70]). Each particle in PSO has a velocity associated with it, which constantly updates depending on the behavior and experience of the particles with others. The expected hypothesis for each update is the arrival of a statistically good number of particles to the same position if the solution is converging, giving the value of local or global optimum. In PSO, each particle is considered a point in a D-dimensional space with the position vector of each i^{th} particle being represented as $X_I = (x_{i1}, x_{i2}, x_{i3}, x_{i4}, ...x_{iD})$, the previous best value of the position (the best position is considered the location where the value of objective function obtained is optimum) being represented by the vector P_I, where $P_I = (p_{i1}, p_{i2}, p_{i3}, p_{i4}, ...p_{iD})$ and the rate of change of position (i.e.velocity), of the i^{th} particle is given by the vector V_I, where $V_I = (v_{i1}, v_{i2}, v_{i3}, v_{i4}, ...v_{iD})$.

$$v_{id} = w * v_{id} + c_1 * rand() * (p_{id} - x_{id}) + c_2 * Rand() * (p_{gd} - x_{id}) \tag{4.1}$$

The update rule followed by the velocity and position of the particles during each iteration is given by Eq. (4.1) and (4.2), respectively, where c_1 and c_2 are two positive constants, rand() and Rand() are two random functions in the range $[0, 1]$, with w as the inertial weight.

$$x_{id} = x_{id} + v_{id} \tag{4.2}$$

Eq. (4.1) provides the new velocity of the particle, which is based on three factors: its previous position, the distance between its current and best position, and lastly, the distance of the particle from the group's best position (here, it takes into account how a larger group of particles experience in the presence of the other particles). Eq. (4.2) shows the new position of the particle, based on the new velocity obtained from Eq. (4.1).

The best behavior or experience of the particles is obtained for the provided objective

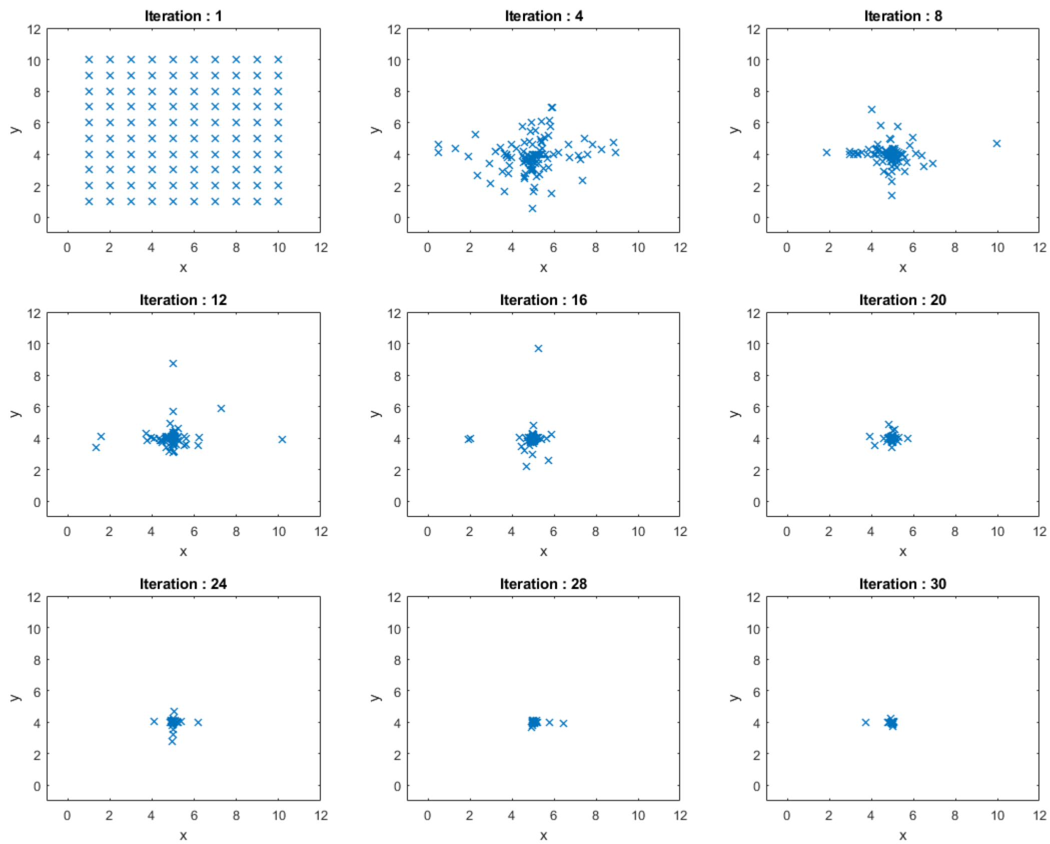

Fig. 4.2 Different iterations while convergence to a solution for minimizing the function $(x-5)^2 + (y-4)^2 = 0$.

function. Based on the initial weights, a global or local optimum is found. Fig. 4.2 shows the convergence to the solution obtained for minimizing the function $(x-5)^2+(y-4)^2=0$ for 30 iterations and 100 particles. The initial position of these particles is shown in iteration 1 of Fig. 4.2. A few iterations showing the behavior of particles during the process of optimization are shown in subplots of Fig. 4.2. It is observed from the final iteration 30 that all particles converge to a smaller area showing the result that the minimum value for the function $(x-5)^2+(y-4)^2=0$ is obtained at the value $x=5$ and $y=4$ along with the minimum value being 0.

4.5 FDTD simulation

Fig. 4.1 shows three regions of the Y-branch: the input port, the central region and the output ports. The region between the input port and the central region is a waveguide with a width of 0.45 μm. The central region of the Y-branch decides the behavior (i.e., performance bandwidth or loss of input field/polarization) of the device and therefore is designed carefully. The objective is to design a Y-branch as a 50-50 splitter with a low insertion loss and constraints on the device's footprint. I used PSO for optimization to have an efficient design of the central region. A complete 3D-FDTD simulation was carried out to run an optimization process. Fig. 4.3(a) shows the simulation setup for the S-bend of the Y-branch and Fig. 4.3(b) shows the transmission profile for a wavelength range of 1500 nm to 1600 nm. In order to arrive at an optimized design, I used PSO to maximize the transmission profile of the S-bend for the source wavelength range of 1500 nm to 1600 nm. The simulation technique for the Y-branch is the same as the one used in [52], which involves slicing the central region of the Y-branch into multiple sections and using a spline interpolation between each slice. As shown in Fig. 4.4, the central region of the Y-branch is divided into 11 slices labeled from $w_1, w_2, w_3.......w_{10}, w_{11}$, along with the width of the waveguide being 450 nm and the separation between the output waveguides of the Y-branch being 250 nm. The entire length, L, of the central region is chosen to be 2 μm and the length of the optimized S-bend is 9 μm. A PSO was performed in the Lumerical FDTD with 50 particles and 30 iterations on a 3.2 GHz octa-core Intel i5 (3^{rd} generation) processor. It took about 15 hours to perform the complete simulation.

The initial seed values for 11 parameters were chosen randomly, and the maximum value of each independent parameter was set to be 2 μm. Since the entire Y-branch is laterally

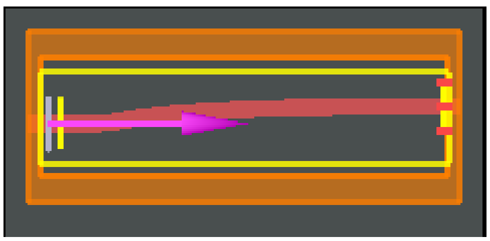

(a)

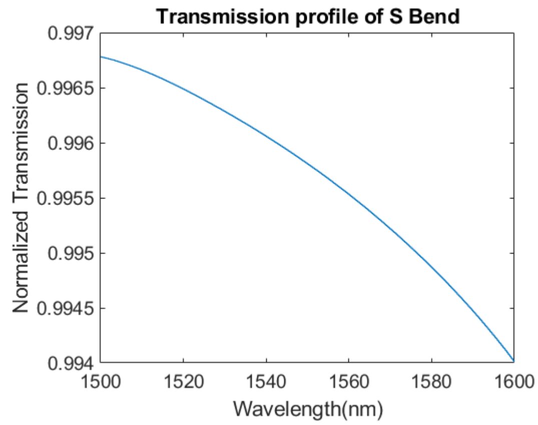

(b)

Fig. 4.3 (a) The simulation region for the S-bend as seen in FDTD, and (b) transmission profile of an optimized S-bend simulated in FDTD.

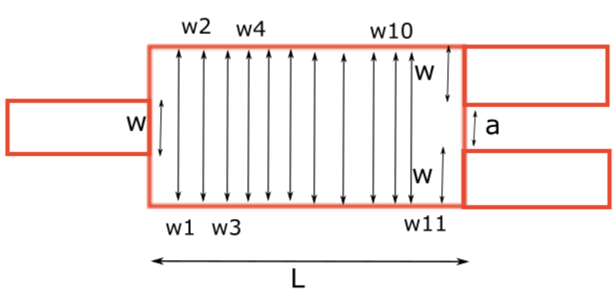

Fig. 4.4 Schematic for designing the Y-branch: $w = 0.45\ \mu m$, $a = 0.25\ \mu m$ and $L = 2\ \mu m$.

symmetrical in order to make the simulations run quickly, this was taken into consideration. After performing the simulation, the optimized values of the 11 parameters are as mentioned in Table 4.1. The transmission profile obtained for the Y-branch corresponding to the parameters mentioned in Table 4.1 is shown in Fig. 4.5. The output obtained from the two branches are almost the same, which indicate equal power splitting.

Table 4.1 Dimensions of the different parameters of optimized Y-branch

Sl. No.	Parameter	Width(μm)
1	w_1	0.65
2	w_2	0.93
3	w_3	1.55
4	w_4	1.37
5	w_5	1.38
6	w_6	1.49
7	w_7	1.53
8	w_8	1.36
9	w_9	1.41
10	w_{10}	1.25
11	w_{11}	1.91

A GDSII layout is sketched for the Y-branch after an optimized design is obtained. Fig. 4.6 shows the GDSII image of the Y-branch fabricated using a 220 nm SOI process. For measurements, the input and output ports of the Y-branch have adjoining grating couplers, as shown in Fig. 4.7.

4.6 Results and Discussion

Initially, the characteristics of the S-bend were studied by measuring the insertion loss. Fig. 4.8(a) shows the transmission spectrum of a grating coupler and S-bend. Fig. 4.8(b) shows the insertion loss of the S-bend after removing the response of the grating coupler. The insertion loss of the S-bend is around 0 dB, with the worst insertion loss of 1.1 dB. A

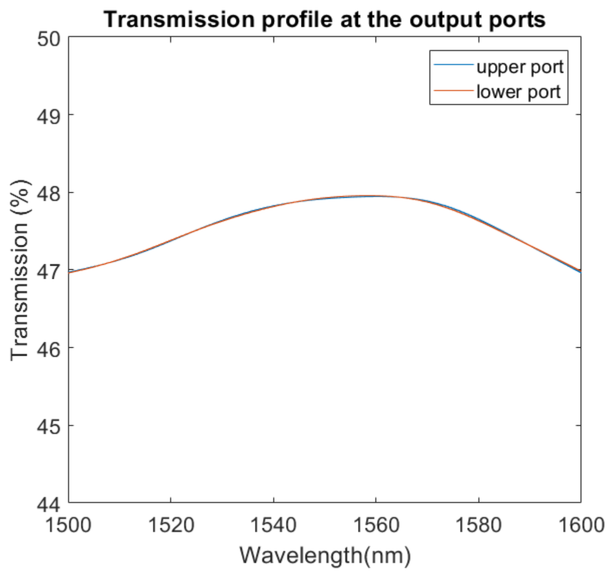

Fig. 4.5 Simulated transmission profile of both the output ports of the optimized Y-branch.

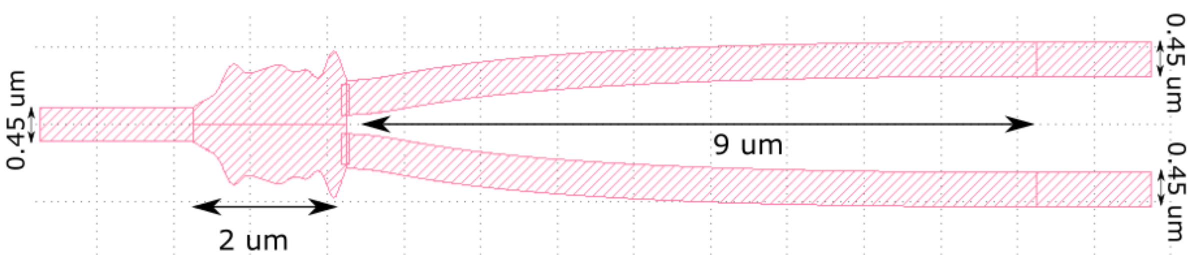

Fig. 4.6 GDSII image of the optimized Y-branch that was fabricated.

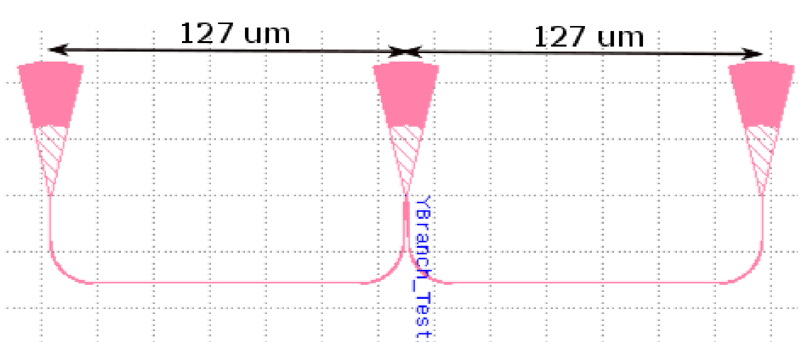

Fig. 4.7 GDSII of the test arrangement for the Y-branch.

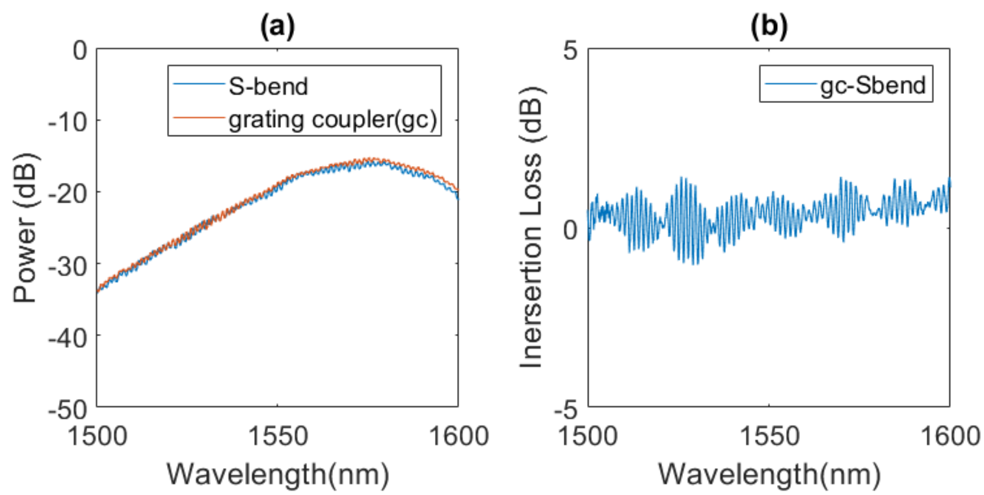

Fig. 4.8 Characterization of the S-bend: (a) the transmission spectra of grating coupler along with S-bend, and (b) the insertion loss of the S-bend (i.e., the response of gc subtracted from the S-bend)

small repeatability test was also conducted to observe whether a similar response would be obtained. In order to have an idea about the repeatability of the S-bend, the insertion losses of four different devices on the same silicon chip were recorded. The spectral responses of these four devices, along with the grating coupler's response, are shown in Fig. 4.9. From the figure, it can be inferred that the response of the S-bend is similar to the grating coupler, indicating negligible insertion loss for the S-bend. Since S-bend is lossless, the Y-branch contributes most of the insertion loss. Also, the Sbend2 response in Fig. 4.9 has some ripples towards the lower wavelength of 1520 nm - 1535 nm. These ripples could be due to fabrication errors or slight error in measurements. In the same figure, the grating coupler and S-bend in response 2 and 4 show a deviation in the wavelength range of 1590 nm - 1600 nm. The maximum and minimum value of the insertion loss for Sbend2 response in this wavelength range is -0.68 dB and -1.68 dB, respectively. In the case of Sbend4 response, the maximum and minimum value of insertion loss is -0.60 dB and -1.87 dB, respectively.

Fig. 4.10(a) shows the spectral response of the output ports of the Y-branch and grating coupler. The spectrum of the Y-branch being lower than that of grating coupler indicates that it has insertion loss. Fig. 4.10(b) shows the splitting ratio of two ports and their

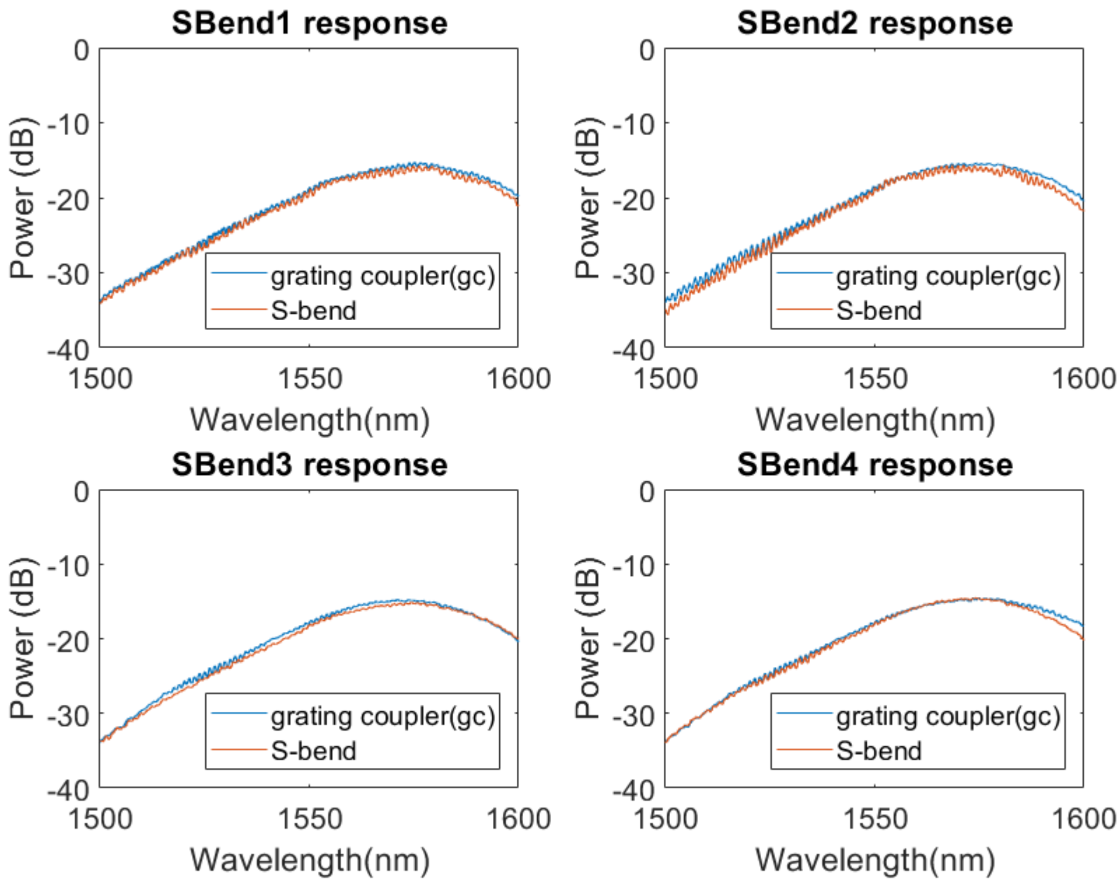

Fig. 4.9 Measured response of the S-bend structures and corresponding grating couplers.

insertion loss. The splitting ratio for the ports is calculated from Eq. (4.3) and (4.4).

$$R_{p1} = \frac{P_1}{P_1 + P_2} \tag{4.3}$$

$$R_{p2} = \frac{P_2}{P_1 + P_2} \tag{4.4}$$

where R_{p1} and R_{p2} are the splitting ratios at port 1 and port 2, respectively. P_1 and P_2 are the power detected at port 1 and 2, respectively. Fig. 4.10(b) indicates a constant splitting ratio throughout the wavelength range of 1500 nm - 1600 nm. The splitting ratio for port 1 ranges from 0.4799 to 0.5142 while the lower port is from 0.4799 to 0.5201. It should be

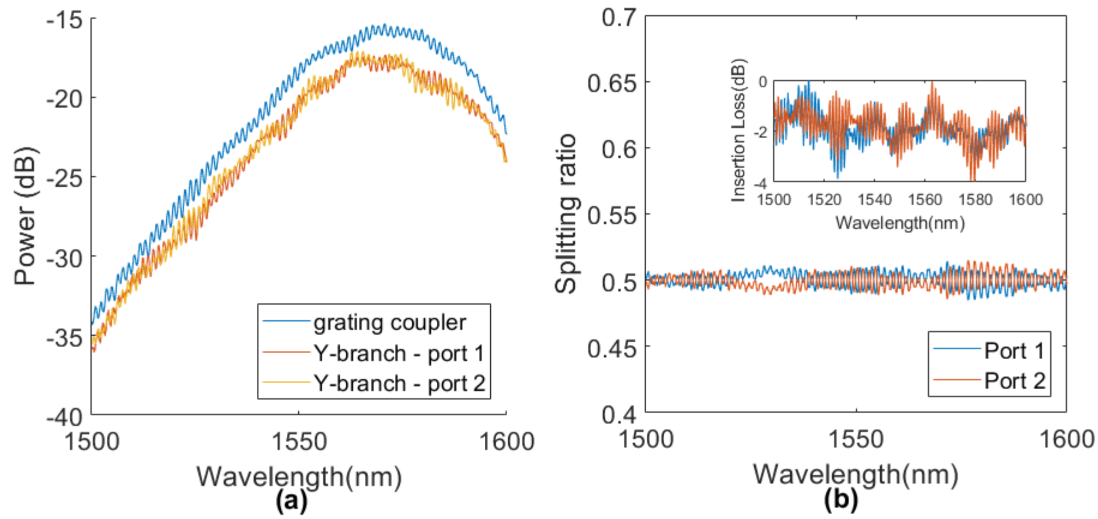

Fig. 4.10 Characterization of the Y-branch: (a) the transmission spectra of grating coupler along with both the ports of the Y-branch, and (b) the splitting ratio of both ports of the Y-branch and inset shows the insertion loss of the two ports.

noted that the insertion loss for both ports is slightly higher (the insertion loss was expected to be around -0.5 dB) than expected because of measurement techniques and fabrication errors. A Y-branch is expected to have low insertion loss (generally around -0.5 dB), which is difficult to measure on a single device structure. To overcome this problem, one can have multiple cascaded Y-branches [52], a combination of which will have increased insertion loss. It is easy and within the experimental limits to measure these increased insertion losses. However, due to the limited space on the chip during fabrication, such an extensive characterization could not be performed.

For testing the repeatability of the Y-branch, three similar design structures were created and splitting ratios were observed. Fig. 4.11 shows the splitting ratio and insertion losses of the two ports of the Y-branch in three different cases with the same design. In Fig. 4.11, the splitting ratio in Y-branch 3 seems to have more variations which could be because of fabrication errors. A summary of the results obtained in three separate cases is presented in Table 4.2. It can be inferred that splitting the ratio remains consistent in all three cases. Also, the spectra of the two output ports overlap over the complete testing wavelength range, indicating balanced output power and wavelength insensitive coupling ratio. Additionally, there are significant insertion losses noted in all the devices. This

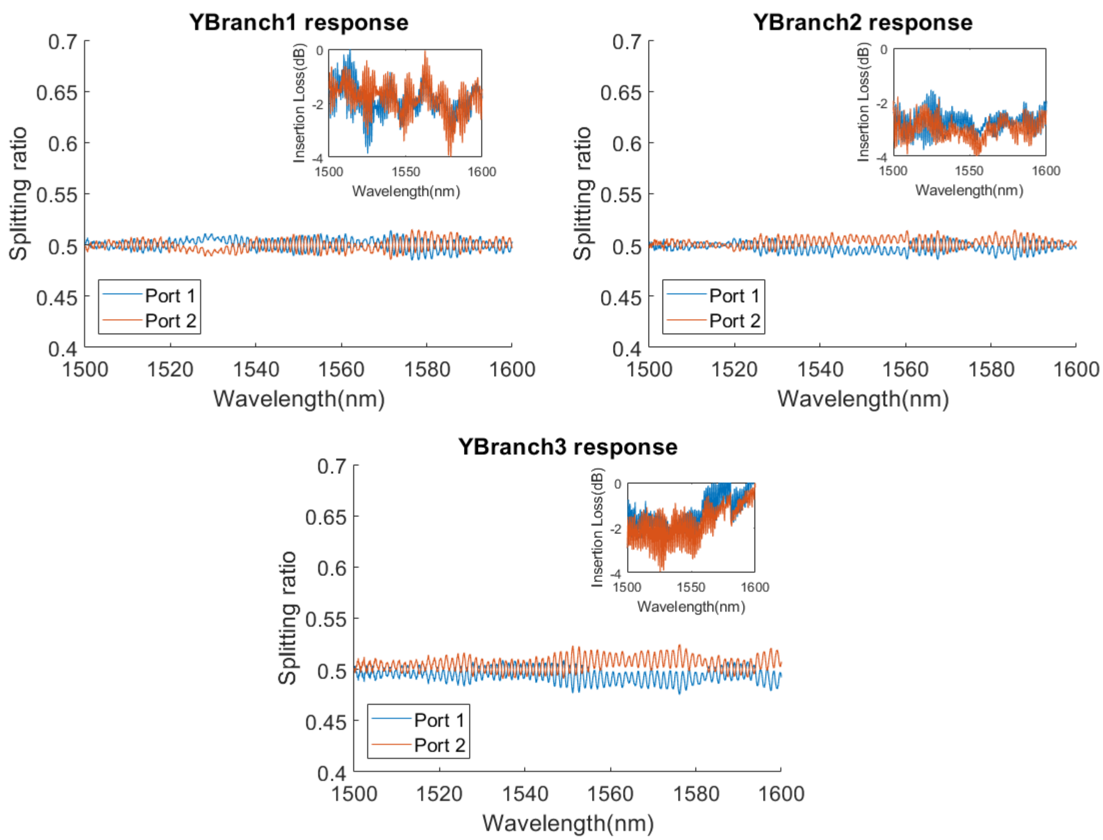

Fig. 4.11 Splitting ratio and measured insertion loss of the Y-branch.

increased IL could be a result of the way the experiment was designed and conducted.

4.7 Future Work

Apart from using PSO for optimization, other algorithms, like a hybrid of PSO with back propagation, can be used in a feed-forward neural network to obtain more accurate results [71, 72, 73]. The accuracy and speed of the results come from the fact that PSO is slower when finding a global optimum compared to gradient descent [71]. Hence, a hybrid of the two can perform a better task. However, for solving inverse problems of obtaining design, the genetic algorithm has proven to be more useful in providing an optimal solution. The complexity of the genetic algorithm is $O(n^2)$, which is higher than that of PSO [74].

Table 4.2 Measurement results of the grating couplers

	Region	Range of splitting ratio	Range of insertion loss
Y-branch 1	Upper Port	[0.4799, 0.5142]	[-3.86 dB, -0.01 dB]
	Lower Port	[0.4858, 0.5201]	[-3.98 dB, -0.05 dB]
Y-branch 2	Upper Port	[0.4854, 0.5089]	[-3.77 dB, -1.54 dB]
	Lower Port	[0.4911, 0.5146]	[-4.24 dB, -1.79 dB]
Y-branch 3	Upper Port	[0.4757, 0.5131]	[-2.92 dB, -0.01 dB]
	Lower Port	[0.4869, 0.5243]	[-3.97 dB, -0.03 dB]

The optimization method can be improved further to implement self-optimizing techniques using machine learning algorithms. The new optimization technique will allow the user to design efficient devices without spending a significant effort to parametrize every geometry. A simple design was carried out on a Y-branch using the self-optimization technique following the L-BFGS-B [75, 76, 77] algorithm. Fig. 4.12 shows a picture of the first step of the optimization along with different gradients computed for various parameters that define the shape of the Y-branch. In Fig. 4.12, FOM determines the quality of the device (in this case, the end goal is to have a FOM of 0.5 for having a 50-50 Y-splitter). Sparse perturbation gradient fields show the changes in the electric field when design parameters (i.e., dimensions of the design), are slightly changed. Parameter evolution shows how different dimensions of geometry change with each iteration differ. The subplot 'Geometry' shows the physical outline of a device. Forward fields E^2 shows the distribution of the propagation of the electric field in the device, while gradient evolution shows how the magnitude of gradients of parameters evolve in each iteration. The gradients in the algorithm are designed to make the performance of the device better with every step. Fig. 4.13 shows the situation when the self-designing simulation has reached convergence in approximately 47 iterations and the electric field splits equally into both branches. The codes used to generate the plots in simulations are from Lumerical's example database [78]. Such advanced algorithms can prove useful for designing devices with little constraints and interferences. Even though these optimizers take considerable running time, the results are obtained without performing any guesswork for geometry. Similar optimization techniques can also be implemented for designing efficient devices in O-band.

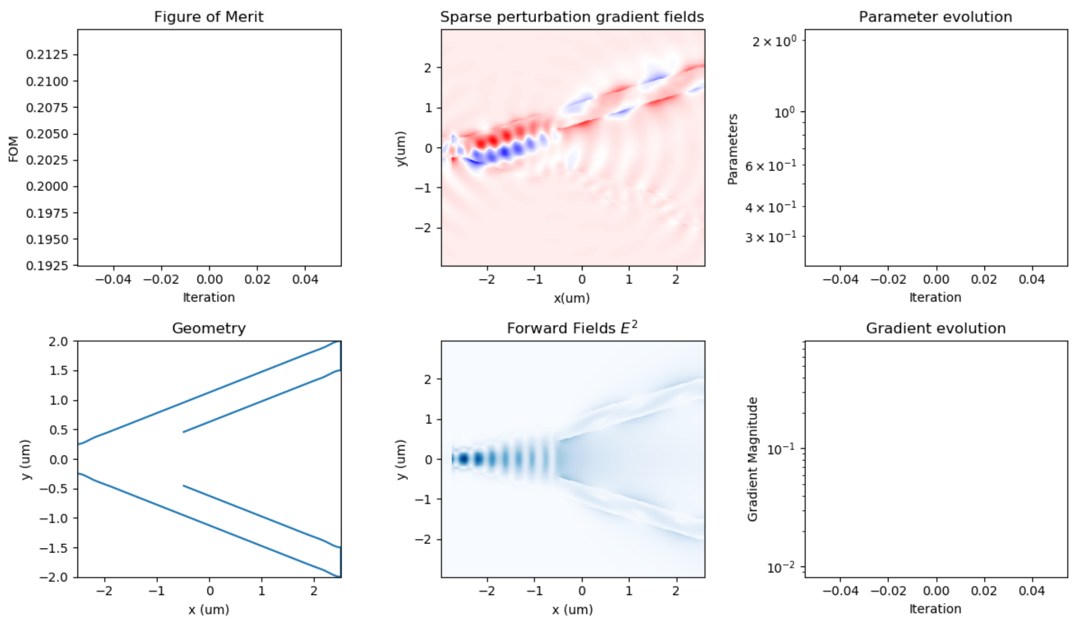

Fig. 4.12 The first iteration of a self-designed Y-branch. Sub-plots Figure of Merit, Parameter evolution, and Gradient evolution are empty as it is the first iteration.

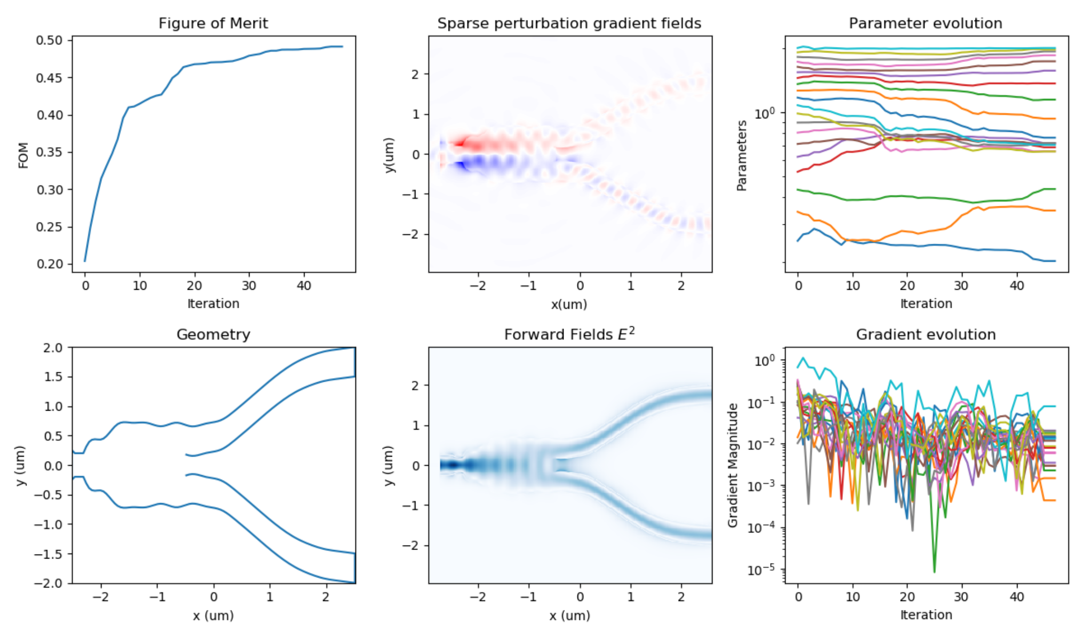

Fig. 4.13 The last iteration step (i.e., the 47^{th}) step of the optimized self-designed Y-branch when all the parameters have converged.

Chapter 5

Conclusion

SiP is one of the most significant technologies to meet the ever-increasing demands in the development of advanced optical devices and high-precision measuring instruments. This demand for low-cost, high precision optical equipment is catalytic in research on devices with high efficiency and performance.

This thesis talks about two important devices: a grating coupler and a Y-branch. Grating couplers were designed to have higher efficiency and reduced back reflections. To some extent, I was successful in achieving this while still maintaining the same 1 dB bandwidth and without an increase in the device footprint. An extra etched section in the tapered region of the coupler helps to suppress the back reflection without compromising the performance of the device. Among the fabricated grating couplers, the best insertion loss was of -4.95 dB, with a 1 dB bandwidth of 93 nm. The results obtained from the three similar devices proved the robustness and repeatability of the device.

With the Y-branch, I analyzed an optimization algorithm that is faster compared to designs created by simple geometrical analysis and sweeping every possible parameter. The method enables a device design with almost the same or better performances than the pre-existing ones. Both ports of the Y-branch have a splitting ratio of 0.5 throughout the wavelength of interest. It can be seen that PSO works efficiently if the objective functions for optimizations are explicitly mentioned.

Besides, the work also contains details regarding a fully automated measurement stage for measuring passive devices. The PaNaMS has been used to test various designs of grating couplers, directional couplers, multi-mode interferometers, hybrids, splitters, wavelength demultiplexers, and adiabatic directional couplers. We have successfully been able to measure six 8 mm x 8 mm chips containing almost 1,000 devices each. The average testing time to measure a single chip with 800 - 1000 devices is approximately five hours, which is a significant reduction in time compared to manual measurements. The development of such a system may not prove useful when measuring a few devices but is of considerable importance in measuring an entire chip containing passive devices. The task of comparing the statistics and characterizing a single or group of devices is also simplified. Repeatability is a crucial factor describing a device, and this feature of the automated stage enables us to have absolute confidence in the devices and their robustness to fabrication errors.

Appendix A

Codes

The appendix contains codes for different parts. A.1 provides the pyxis code and ample file for drawing all the different variations of the grating couplers. A.2 contains MATLAB codes for the analysis of a simple PSO optimization. A.3 contains link to all the codes used to build PaNaMS along with the driver files required. It also explains the working and hierarchical structure of the codes.

A.1 Layout Drawing

```
function Device_Broadband_SWGC_SWtap(query: optional boolean {default = false}),INVISIBLE
{
    if(query) { return[@point, @block, []] }
        local device = $get_device_iobj();
        local wl = $get_property_value(device,"wl");        // operational wavelength
    local n_clad = $get_property_value(device,"n_clad");        // index of the cladding material
    local polarization = $get_property_value(device,"polarization");    // polarization of the ligth you are interested
    local period = $get_property_value(device,"period");                // period of the grating
```

```
    local period_t = $get_property_value(device,"period_t");                    // period of the taper
    local ff = $get_property_value(device,"ff");
    local ff_t = $get_property_value(device,"ff_t");
    local ff_h = $get_property_value(device,"ff_h");
    local ff_l = $get_property_value(device,"ff_l");
    local N_h = $get_property_value(device,"N_h");
    local N_l = $get_property_value(device,"N_l");
   local wg_width = $get_property_value(device,"wg_width");              // waveguide width
          local taper_length = $get_property_value(device,"taper_length");              // taper length
    local incident_angle = $get_property_value(device,"incident_angle");     // incident angle of the input light
    local N = $get_property_value(device,"N");                                  // integer determines the position of the first grating
          build_Device_Broadband_SWGC_SWtap(wl,n_clad,polarization,period,period_t,ff,ff_t,ff_h,ff_l,N_h,N_l,wg_width,taper_length,incident_angle,N);
}
function build_Device_Broadband_SWGC_SWtap(wl:number {default=1.55},n_clad:number {default=1.44},polarization:string {default="TE"},\
 period:number {default=1.13},period_t:number {default=0.05},ff:number {default=0.5},ff_t:number {default=0.75}, ff_h:number {default=0.49},ff_l:number {default=0.13},N_h:number {default=3},N_l:number {default=2},\
wg_width:number {default=0.5},taper_length:number {default=25},incident_angle:number {default=25},\
N:number {default=26})
{
    //Save Original user settings
```

```
        local selectable_types_orig = $get_selectable_types();
        local selectable_layers_orig = $get_selectable_layers();
        local autoselect_orig = $get_autoselect();

        //Set up selection settings
        $set_selectable_types(@replace, [@shape, @path, @pin,
           @overflow,@row, @property_text, @instance, @array,
           @device, @via_object, @text, @region,
        @bisector, @channel, @slice], @both);
        $set_selectable_layers(@replace, ["0-4096"]);
        $set_autoselect(@true);



   local ne=0;
   local segnum=200;
   local seg_points = segnum+1;
   local nf =1;      // fiber mode
        local arc_vec = $create_vector(2*seg_points);
   local arc_vec_sub = $create_vector(2*seg_points);
   local taper_vec = $create_vector(2*seg_points);
        local end_taper_vec = $create_vector(seg_points+2);
   local e=0;
  // local N=0;
   local angle_e=28;
   local gc_number=$round(22/period);
        local i = 0;
        local ii=0;
   local j = 0;
   local k = 0;
   local x_r=0;
        local y_r=0;
        local x_l=0;
```

```
        local y_l=0;
    local t_lx=0;
    local t_ly=0;
        local t_rx = 0;
        local t_ry = 0;
    local x_r_sub=0;
        local y_r_sub=0;
        local x_l_sub=0;
        local y_l_sub=0;
    local r_h=0;
    local r_l=0;
    local r_taper=0;
    local duty_cycle=(period*ff*ff_h+period*(1-ff)*ff_l)/period;
    local neff_TE=0;
    local neff_TM=0;
    local NL=0;
    local NH=0;

    if (polarization=="TE") {
     neff_TE=-0.0013*wl*1000+4.4;      // wavelength dependant
        effective index for fundamental TE
     ne=neff_TE*duty_cycle+(1-duty_cycle)*n_clad;
     $writes_file($stdout,"ne=",ne);
     }
    else {
      neff_TM=-0.0012*wl*1000+3.5;      // wavelength dependant
         effective index for fundamental TM
      ne=neff_TM*duty_cycle+(1-duty_cycle)*n_clad;
      $writes_file($stdout,"ne=",ne);
     }

    e =nf*sin(rad(abs(incident_angle)))/ne;
    $writes_file($stdout,"e=",e);
```

```
  //  N=$round((30+period-g_width)*(1+e)*ne/wl);
  //     N=$round((30+period-g_width)*(1-e)*ne/wl);       // for
     tapers using the furthur foci;




local sub_h=period*ff/N_h*ff_h;      // width of the sub-
    wavelength grating in the low index region
local sub_l=period*(1-ff)/N_l*ff_l;  // width of the sub-
    wavelength grating in the high index region

local sec_h=period*ff/N_h;      // width of one sub-wavelength
    region in the low index region
local sec_l=period*(1-ff)/N_l;  // width of one sub-wavelength
    region in the high index region


    for(j=0;j<gc_number;j=j+1)
        {

     for  (NL=0;NL<N_l;  NL=NL+1)
           {

           for(i=0;i<seg_points;i=i+1)
                {

              r=(N*wl/ne)/(1-e*cos(rad(-angle_e/2+angle_e/segnum*i))
                  );
              x_l=(r-period*(1-ff)+sec_l/2-0.5*sub_l+NL*sec_l+j*
                  period)*cos(rad(-angle_e/2+angle_e/segnum*i));
```

```
            y_l=(r-period*(1-ff)+sec_l/2-0.5*sub_l+NL*sec_l+j*
                period)*sin(rad(-angle_e/2+angle_e/segnum*i));
                    arc_vec[i] = [x_l,y_l];

            x_r=(r-period*(1-ff)+sec_l/2+0.5*sub_l+NL*sec_l+j*
                period)*cos(rad(angle_e/2-angle_e/segnum*i));
            y_r=(r-period*(1-ff)+sec_l/2+0.5*sub_l+NL*sec_l+j*
                period)*sin(rad(angle_e/2-angle_e/segnum*i));
                    arc_vec[seg_points+i] = [x_r,y_r];


                }  // end loop for i

                 $add_shape(arc_vec,"Si");
                }  // end loop for NL

        for (NH=0;NH<N_h; NH=NH+1)
          {
            for(ii=0;ii<seg_points;ii=ii+1)
                {

            r_h=(N*wl/ne)/(1-e*cos(rad(-angle_e/2+angle_e/segnum*
                ii)));

            x_l_sub=(r_h+sec_h/2+NH*sec_h-0.5*sub_h+j*period)*cos(
                rad(-angle_e/2+angle_e/segnum*ii));
            y_l_sub=(r_h+sec_h/2+NH*sec_h-0.5*sub_h+j*period)*sin(
                rad(-angle_e/2+angle_e/segnum*ii));
                    arc_vec_sub[ii] = [x_l_sub,y_l_sub];

            x_r_sub=(r_h+sec_h/2+NH*sec_h+0.5*sub_h+j*period)*cos(
                rad(angle_e/2-angle_e/segnum*ii));
```

```
            y_r_sub=(r_h+sec_h/2+NH*sec_h+0.5*sub_h+j*period)*sin(
                rad(angle_e/2-angle_e/segnum*ii));
                        arc_vec_sub[seg_points+ii] = [x_r_sub,
                            y_r_sub];

                    }  // end loop for i

                $add_shape(arc_vec_sub,"Si");

                }  // end loop for NH


    //  arc_vec=$round(arc_vec/0.005)*0.005;


    }    // end loop for j



        local gc_number_t=$round(taper_length/period_t);
        local sub_t=period_t*(ff_t);  // width of the sub-
            wavelength grating in the taper region
        local sec_t=period_t*(1);  // width of one sub-wavelength
             region in the taper region

        for(j=0;j<=gc_number_t;j=j+1)
     {
         for(i=0;i<seg_points;i=i+1)
                {
            //version 1
            //r_h=(0.5*wl/ne)/(1-e*cos(rad(angle_e/2-angle_e/
                segnum*i)));

```

```
            //x_l_sub=(r_h+sec_t/2-0.5*sub_t+j*period_t)*cos(rad(angle_e/2-angle_e/segnum*i));
            //y_l_sub=(r_h+sec_t/2-0.5*sub_t+j*period_t)*sin(rad(-angle_e/2+angle_e/segnum*i));
                    //taper_vec[i] = [x_l_sub,y_l_sub];

            //x_r_sub=(r_h+sec_t/2+0.5*sub_t+j*period_t)*cos(rad(angle_e/2-angle_e/segnum*i));
            //y_r_sub=(r_h+sec_t/2+0.5*sub_t+j*period_t)*sin(rad(angle_e/2-angle_e/segnum*i));
                    //taper_vec[seg_points+i] = [x_r_sub,y_r_sub];


                            //version 2

                            //r=(0.5*wl/ne)/(1-e*cos(rad(-angle_e/2+angle_e/segnum*i)));
            //x_l=(r-period_t*(1-ff_t)+sec_t/2-0.5*sub_t+sec_t+j*period)*cos(rad(-angle_e/2+angle_e/segnum*i));
            //y_l=(r-period_t*(1-ff_t)+sec_t/2-0.5*sub_t+sec_t+j*period)*sin(rad(-angle_e/2+angle_e/segnum*i));
                    //taper_vec[i] = [x_l,y_l];

            //x_r=(r-period_t*(1-ff_t)+sec_t/2+0.5*sub_t+sec_t+j*period)*cos(rad(angle_e/2-angle_e/segnum*i));
           //  y_r=(r-period_t*(1-ff_t)+sec_t/2+0.5*sub_t+sec_t+j*period)*sin(rad(angle_e/2-angle_e/segnum*i));
                   //  taper_vec[seg_points+i] = [x_r,y_r];


                            //version 3
```

```
                    r_taper=(N*wl/ne)/(1-e*cos(rad(
                        angle_e/2-angle_e/segnum*i)));
                    if(j==gc_number_t)
                    {
                            t_lx=(r_taper-period*(1-
                                ff)-j*period_t)*cos(
                                rad(angle_e/2-angle_e/
                                segnum*i));
            t_ly=(r_taper-period*(1-ff)-j*period_t)*sin
                (rad(angle_e/2-angle_e/segnum*i));
                        end_taper_vec[i] = [t_lx,t_ly
                            ];
                    }
                    else
                    {
                t_lx=(r_taper-period*(1-ff)-j*period_t)*
                    cos(rad(angle_e/2-angle_e/segnum*i));
            t_ly=(r_taper-period*(1-ff)-j*period_t)*sin
                (rad(angle_e/2-angle_e/segnum*i));
                        taper_vec[i] = [t_lx,t_ly];

                            t_rx=(r_taper-period*(1-
                                ff)-period_t*ff_t-j*
                                period_t)*cos(rad(-
                                angle_e/2+angle_e/
                                segnum*i));
        t_ry=(r_taper-period*(1-ff)-period_t*ff_t-j*
            period_t)*sin(rad(-angle_e/2+angle_e/segnum*i)
            );
                        taper_vec[seg_points+i] = [
                            t_rx,t_ry];
                    }

```

```
                } // end loop for i
                        $add_shape(taper_vec,"Si");

        }



//          end_taper_vec[seg_points] = [0,0+1/2*wg_width];
//          end_taper_vec[seg_points+1] = [0,0-1/2*wg_width];
          end_taper_vec[seg_points] = [0,0-1/2*wg_width];          //
             for confocal ellipses orginates at F1;
          end_taper_vec[seg_points+1] = [0,0+1/2*wg_width];


//          taper_vec[seg_points] = [0,0+1/2*wg_width];
//          taper_vec[seg_points+1] = [0,0-1/2*wg_width];
        // taper_vec[seg_points] = [0,0-1/2*wg_width];          //
             for confocal ellipses orginates at F1;
          //taper_vec[seg_points+1] = [0,0+1/2*wg_width];


   // taper_vec=$round(taper_vec/0.005)*0.005;
   $add_shape(end_taper_vec,"Si");


   //$unselect_all(@nofilter);
        $add_shape([[1, -wg_width/2], [0, wg_width/2]], "Si",
           @internal); //Metal routing



        //Restore original user settings
```

```
        $set_selectable_types(@replace, (selectable_types_orig[0]==void)?[]:selectable_types_orig[0], selectable_types_orig[1]);
        $set_selectable_layers(@replace, selectable_layers_orig);
        $set_autoselect(autoselect_orig);

}

function Device_Broadband_SWGC_SWtap_parameters( wl:optional number {default=1.55},n_clad:optional number {default=1.44},\
polarization:optional string {default="TE"},period:optional number {default=1.13},period_t:optional number {default=0.07},ff:optional number {default=0.5},ff_t:optional number {default=0.75},\
ff_h:optional number {default=0.49},ff_l:optional number {default=0.13},N_h:optional number {default=3},N_l:optional number {default=2},\
wg_width:optional number {default=0.5},taper_length:optional number {default=25},incident_angle:optional number {default=22},N:optional number {default=26})
{ return [ ["wl",$g(wl)],["n_clad",$g(n_clad)],["polarization",polarization],["period",$g(period)],["period_t",$g(period_t)],["ff",$g(ff)],["ff_t",$g(ff_t)],["ff_h",$g(ff_h)],\
["ff_l",$g(ff_l)],["N_h",$g(N_h)],["N_l",$g(N_l)],["wg_width",$g(wg_width)],["taper_length",$g(taper_length)],["incident_angle",$g(incident_angle)],["N",$g(N)] ]; }
```

A.2 PSO analysis

```
clear
clc
iterations = 30;
inertia = 1.0;
```

```
correction_factor = 2.0;
swarm_size = 100;

% ---- initial position of swarms-----
index = 1;
for i = 1 : 10
    for j = 1 : 10
        swarm(index, 1, 1) = i;
        swarm(index, 1, 2) = j;
        index = index + 1;
    end
end

swarm(:, 4, 1) = 1000;          % best value so far
swarm(:, 2, :) = 0;             % initial velocity
figure;
j=1;
for iter = 1 : iterations


    for i = 1 : swarm_size
        swarm(i, 1, 1) = swarm(i, 1, 1) + swarm(i, 2, 1)/1.3;
        swarm(i, 1, 2) = swarm(i, 1, 2) + swarm(i, 2, 2)/1.3;
        x = swarm(i, 1, 1);
        y = swarm(i, 1, 2);

        val = (x - 5)^4 + (y - 4)^2;          % function to be
            minimized


        if val < swarm(i, 4, 1)
            swarm(i, 3, 1) = swarm(i, 1, 1);
            swarm(i, 3, 2) = swarm(i, 1, 2);
```

```
                swarm(i, 4, 1) = val;
            end
        end

        [temp, gbest] = min(swarm(:, 4, 1));
        %-- updating velocity vectors
        for i = 1 : swarm_size
            swarm(i, 2, 1) = rand*inertia*swarm(i, 2, 1) + correction_factor*rand*(swarm(i, 3, 1) - swarm(i, 1, 1)) + correction_factor*rand*(swarm(gbest, 3, 1) - swarm(i, 1, 1));   %x velocity component
            swarm(i, 2, 2) = rand*inertia*swarm(i, 2, 2) + correction_factor*rand*(swarm(i, 3, 2) - swarm(i, 1, 2)) + correction_factor*rand*(swarm(gbest, 3, 2) - swarm(i, 1, 2));   %y velocity component
        end

        %% Plotting the swarm
        %clf
        if(mod(iter,4)==0 || iter==1 || iter==30)
        subplot(3,3,j)

        plot(swarm(:, 1, 1), swarm(:, 1, 2), 'x')   %
        title(['Iteration : ',num2str(iter)])
        xlabel('x');
        ylabel('y');
        axis([-1 12 -1 12]);
        j=j+1;
        end

pause(.2)
end
```

A.3 PaNaMS

The code can be found at the link: https://github.com/Amarkr1/Automated-Stage. Before executing the code one needs to ensure that all the hardware is properly connected and functional.

References

[1] A. Bianco, D. Camerino, D. Cuda, and F. Neri, "Optics vs. electronics in future high-capacity switches/routers," in *High Performance Switching and Routing, 2009. HPSR 2009. International Conference on*, pp. 1–6, IEEE, 2009.

[2] A. J. DeMaria, "Photonics vs. electronics technologies," *Optics News*, vol. 15, no. 4, pp. 22–37, 1989.

[3] A. Joshi, C. Batten, Y.-J. Kwon, S. Beamer, I. Shamim, K. Asanovic, and V. Stojanovic, "Silicon-photonic clos networks for global on-chip communication," in *2009 3rd ACM/IEEE International Symposium on Networks-on-Chip*, pp. 124–133, IEEE, 2009.

[4] D. Schall, D. Neumaier, M. Mohsin, B. Chmielak, J. Bolten, C. Porschatis, A. Prinzen, C. Matheisen, W. Kuebart, B. Junginger, *et al.*, "50 gbit/s photodetectors based on wafer-scale graphene for integrated silicon photonic communication systems," *ACS Photonics*, vol. 1, no. 9, pp. 781–784, 2014.

[5] M. Iqbal, M. A. Gleeson, B. Spaugh, F. Tybor, W. G. Gunn, M. Hochberg, T. Baehr-Jones, R. C. Bailey, and L. C. Gunn, "Label-free biosensor arrays based on silicon ring resonators and high-speed optical scanning instrumentation," *IEEE Journal of Selected Topics in Quantum Electronics*, vol. 16, no. 3, pp. 654–661, 2010.

[6] S. Srinivasan, R. Moreira, D. Blumenthal, and J. E. Bowers, "Design of integrated hybrid silicon waveguide optical gyroscope," *Optics Express*, vol. 22, no. 21, pp. 24988–24993, 2014.

[7] B. Yu, H. Wang, A. Joshi, Q. Xiang, E. Ibok, and M.-R. Lin, "15 nm gate length planar cmos transistor," in *Electron Devices Meeting, 2001. IEDM'01. Technical Digest. International*, pp. 11–7, IEEE, 2001.

[8] S. Cova, M. Ghioni, A. Lacaita, C. Samori, and F. Zappa, "Avalanche photodiodes and quenching circuits for single-photon detection," *Applied Optics*, vol. 35, no. 12, pp. 1956–1976, 1996.

[9] R. J. McIntyre, "The distribution of gains in uniformly multiplying avalanche photodiodes: Theory," *IEEE Transactions on Electron Devices*, vol. 19, no. 6, pp. 703–713, 1972.

[10] T. Ishibashi, N. Shimizu, S. Kodama, H. Ito, T. Nagatsuma, and T. Furuta, "Uni-traveling-carrier photodiodes," in *Ultrafast Electronics and Optoelectronics*, p. UC3, Optical Society of America, 1997.

[11] R. Soref, "The past, present, and future of silicon photonics," *IEEE Journal of selected topics in quantum electronics*, vol. 12, no. 6, pp. 1678–1687, 2006.

[12] D. Inniss and R. Rubenstein, *Silicon Photonics: Fueling the Next Information Revolution*. Morgan Kaufmann, 2016.

[13] H. Subbaraman, X. Xu, A. Hosseini, X. Zhang, Y. Zhang, D. Kwong, and R. T. Chen, "Recent advances in silicon-based passive and active optical interconnects," *Optics Express*, vol. 23, no. 3, pp. 2487–2511, 2015.

[14] Z. Zhou, B. Yin, and J. Michel, "On-chip light sources for silicon photonics," *Light: Science & Applications*, vol. 4, no. 11, p. e358, 2015.

[15] W. Bogaerts, R. Baets, P. Dumon, V. Wiaux, S. Beckx, D. Taillaert, B. Luyssaert, J. Van Campenhout, P. Bienstman, and D. Van Thourhout, "Nanophotonic waveguides in silicon-on-insulator fabricated with cmos technology," *Journal of Lightwave Technology*, vol. 23, no. 1, p. 401, 2005.

[16] I. Malitson, "Interspecimen comparison of the refractive index of fused silica," *Journal of the Optical Society of America*, vol. 55, no. 10, pp. 1205–1209, 1965.

[17] H. Li, "Refractive index of silicon and germanium and its wavelength and temperature derivatives," *Journal of Physical and Chemical Reference Data*, vol. 9, no. 3, pp. 561–658, 1980.

[18] L. Zhu, W. Yang, and C. Chang-Hasnain, "Very high efficiency optical coupler for silicon nanophotonic waveguide and single mode optical fiber," *Optics Express*, vol. 25, no. 15, pp. 18462–18473, 2017.

[19] P. Markov, J. G. Valentine, and S. M. Weiss, "Fiber-to-chip coupler designed using an optical transformation," *Optics Express*, vol. 20, no. 13, pp. 14705–14713, 2012.

[20] G. T. Reed and A. P. Knights, *Silicon photonics: an introduction*. John Wiley & Sons, 2004.

[21] L. Chrostowski and M. Hochberg, *Silicon photonics design: from devices to systems*. Cambridge University Press, 2015.

[22] N. Na, H. Frish, I.-W. Hsieh, O. Harel, R. George, A. Barkai, and H. Rong, "Efficient broadband silicon-on-insulator grating coupler with low backreflection," *Optics Letters*, vol. 36, no. 11, pp. 2101–2103, 2011.

[23] D. Vermeulen, Y. De Koninck, Y. Li, E. Lambert, W. Bogaerts, R. Baets, and G. Roelkens, "Reflectionless grating coupling for silicon-on-insulator integrated circuits," in *Group IV Photonics (GFP), 2011 8th IEEE International Conference on*, pp. 74–76, IEEE, 2011.

[24] P. Lalanne and J.-P. Hugonin, "High-order effective-medium theory of subwavelength gratings in classical mounting: application to volume holograms," *Journal of the Optical Society of America A*, vol. 15, no. 7, pp. 1843–1851, 1998.

[25] S. Rytov, "Electromagnetic properties of a finely stratified medium," *Soviet Physics JEPT*, vol. 2, pp. 466–475, 1956.

[26] R. Halir, P. J. Bock, P. Cheben, A. Ortega-Moñux, C. Alonso-Ramos, J. H. Schmid, J. Lapointe, D.-X. Xu, J. G. Wangüemert-Pérez, Í. Molina-Fernández, *et al.*, "Waveguide sub-wavelength structures: a review of principles and applications," *Laser & Photonics Reviews*, vol. 9, no. 1, pp. 25–49, 2015.

[27] J. G. Wangüemert-Pérez, A. Hadij-ElHouati, A. Sánchez-Postigo, J. Leuermann, D.-X. Xu, P. Cheben, A. Ortega-Moñux, R. Halir, and Í. Molina-Fernández, "Subwavelength structures for silicon photonics biosensing," *Optics & Laser Technology*, vol. 109, pp. 437–448, 2019.

[28] P. Cheben, J. Čtyrokỳ, J. H. Schmid, S. Wang, J. Lapointe, J. G. Wangüemert-Pérez, Í. Molina-Fernández, A. Ortega-Moñux, R. Halir, D. Melati, *et al.*, "Bragg filter bandwidth engineering in subwavelength grating metamaterial waveguides," *Optics Letters*, vol. 44, no. 4, pp. 1043–1046, 2019.

[29] D. González-Andrade, J. G. Wangüemert-Pérez, A. V. Velasco, A. Ortega-Moñux, A. Herrero-Bermello, I. Molina-Fernández, R. Halir, and P. Cheben, "Ultra-broadband mode converter and multiplexer based on sub-wavelength structures," *IEEE Photonics Journal*, vol. 10, no. 2, pp. 1–10, 2018.

[30] H. Kikuta, H. Toyota, and W. Yu, "Optical elements with subwavelength structured surfaces," *Optical Review*, vol. 10, no. 2, pp. 63–73, 2003.

[31] C. F. Mateus, M. C. Huang, L. Chen, C. J. Chang-Hasnain, and Y. Suzuki, "Broadband mirror (1.12-1.62 μm) using a subwavelength grating," *IEEE Photonics Technology Letters*, vol. 16, no. 7, pp. 1676–1678, 2004.

[32] J. Schmid, P. Cheben, S. Janz, J. Lapointe, E. Post, A. Delâge, A. Densmore, B. Lamontagne, P. Waldron, and D.-X. Xu, "Subwavelength grating structures in silicon-on-insulator waveguides," *Advances in Optical Technologies*, vol. 2008, 2008.

[33] J. Schmid, P. Cheben, S. Janz, J. Lapointe, E. Post, and D.-X. Xu, "Gradient-index antireflective subwavelength structures for planar waveguide facets," *Optics Letters*, vol. 32, no. 13, pp. 1794–1796, 2007.

[34] P. J. Bock, P. Cheben, J. H. Schmid, J. Lapointe, A. Delâge, D.-X. Xu, S. Janz, A. Densmore, and T. J. Hall, "Subwavelength grating crossings for silicon wire waveguides," *Optics Express*, vol. 18, no. 15, pp. 16146–16155, 2010.

[35] X. Chen, C. Li, C. K. Fung, S. M. Lo, and H. K. Tsang, "Apodized waveguide grating couplers for efficient coupling to optical fibers," *IEEE Photonics Technology Letters*, vol. 22, no. 15, pp. 1156–1158, 2010.

[36] Y. Zhang, T. Baehr-Jones, R. Ding, T. Pinguet, Z. Xuan, and M. Hochberg, "Silicon multi-project wafer platforms for optoelectronic system integration," in *The 9th International Conference on Group IV Photonics (GFP)*, pp. 63–65, IEEE, 2012.

[37] G. Roelkens, D. Vermeulen, D. Van Thourhout, R. Baets, S. Brision, P. Lyan, P. Gautier, and J.-M. Fedeli, "High efficiency diffractive grating couplers for interfacing a single mode optical fiber with a nanophotonic silicon-on-insulator waveguide circuit," *Applied Physics Letters*, vol. 92, no. 13, p. 131101, 2008.

[38] D. Taillaert, P. Bienstman, and R. Baets, "Compact efficient broadband grating coupler for silicon-on-insulator waveguides," *Optics Letters*, vol. 29, no. 23, pp. 2749–2751, 2004.

[39] H. Zhang, C. Li, X. Tu, J. Song, H. Zhou, X. Luo, Y. Huang, M. Yu, and G. Lo, "Efficient silicon nitride grating coupler with distributed bragg reflectors," *Optics Express*, vol. 22, no. 18, pp. 21800–21805, 2014.

[40] D. Vermeulen, S. Selvaraja, P. Verheyen, G. Lepage, W. Bogaerts, P. Absil, D. Van Thourhout, and G. Roelkens, "High-efficiency fiber-to-chip grating couplers realized using an advanced cmos-compatible silicon-on-insulator platform," *Optics Express*, vol. 18, no. 17, pp. 18278–18283, 2010.

[41] C. F. Mateus, M. C. Huang, Y. Deng, A. R. Neureuther, and C. J. Chang-Hasnain, "Ultrabroadband mirror using low-index cladded subwavelength grating," *IEEE Photonics Technology Letters*, vol. 16, no. 2, pp. 518–520, 2004.

[42] R. Halir, P. Cheben, J. Schmid, R. Ma, D. Bedard, S. Janz, D.-X. Xu, A. Densmore, J. Lapointe, and I. Molina-Fernández, "Continuously apodized fiber-to-chip surface

grating coupler with refractive index engineered subwavelength structure," *Optics Letters*, vol. 35, no. 19, pp. 3243–3245, 2010.

[43] J. Kang, Z. Cheng, W. Zhou, T.-H. Xiao, K.-L. Gopalakrisna, M. Takenaka, H. K. Tsang, and K. Goda, "Focusing subwavelength grating coupler for mid-infrared suspended membrane germanium waveguides," *Optics Letters*, vol. 42, no. 11, pp. 2094–2097, 2017.

[44] D. Benedikovic, P. Cheben, J. H. Schmid, D.-X. Xu, J. Lapointe, S. Wang, R. Halir, A. Ortega-Moñux, S. Janz, and M. Dado, "High-efficiency single etch step apodized surface grating coupler using subwavelength structure," *Laser & Photonics Reviews*, vol. 8, no. 6, pp. L93–L97, 2014.

[45] Y. Wang, W. Shi, X. Wang, Z. Lu, M. Caverley, R. Bojko, L. Chrostowski, and N. A. Jaeger, "Design of broadband subwavelength grating couplers with low back reflection," *Optics Letters*, vol. 40, no. 20, pp. 4647–4650, 2015.

[46] X. Chen, K. Xu, Z. Cheng, C. K. Fung, and H. K. Tsang, "Wideband subwavelength gratings for coupling between silicon-on-insulator waveguides and optical fibers," *Optics Letters*, vol. 37, no. 17, pp. 3483–3485, 2012.

[47] F. Lumerical, "Lumerical solutions." Available at https://www.lumerical.com/products/#device.

[48] Lumerical, *Grating Coupler 3-D FDTD*. Available at https://apps.lumerical.com/pic_passive_grating_coupler_3d.html.

[49] Lumerical, *Lumerical's 2.5D FDTD Propagation Method*. Available at https://www.lumerical.com/learn/whitepapers/lumericals-2-5d-fdtd-propagation-method/.

[50] Y. Wang, "Grating coupler design based on silicon-on-insulator," Master's thesis, University of British Columbia, 2013.

[51] Y. Wang, L. Xu, A. Kumar, D. Patel, Z. Xing, R. Li, M. G. Saber, Y. D'Mello, E. El-Fiky, and D. V. Plant, "Broadband sub-wavelength grating coupler for o-band application," in *2017 IEEE 14th International Conference on Group IV Photonics (GFP)*, pp. 129–130, IEEE, 2017.

[52] Y. Zhang, S. Yang, A. E.-J. Lim, G.-Q. Lo, C. Galland, T. Baehr-Jones, and M. Hochberg, "A compact and low loss y-junction for submicron silicon waveguide," *Optics Express*, vol. 21, no. 1, pp. 1310–1316, 2013.

[53] N. Goto and G. Yip, "Y-branch wavelength multi/demultiplexer for gamma= 1.30 and 1.55 mu m," *Electronics Letters*, vol. 26, no. 2, pp. 102–103, 1990.

[54] T. Hoekstra, H. Van Weerden, P. Lambeck, and T. J. Popma, "Bent asymmetric y-branch integrated optical broadband wavelength multi/demultiplexer," *IEEE Photonics technology letters*, vol. 6, no. 1, pp. 83–85, 1994.

[55] L. Li, G. Liu, and H. Lu, "A y-branch demultiplexer based on kagomé lattice photonic crystals," *Optik-International Journal for Light and Electron Optics*, vol. 124, no. 17, pp. 2913–2915, 2013.

[56] K. Kintaka, J. Nishii, S. Yamaguchi, T. Kobayashi, and S. Ura, "Vertically y-branched mode splitter/combiner for intraboard chip-to-chip optical interconnection with wavelength-division multiplexing," *Japanese Journal of Applied Physics*, vol. 46, no. 8S, p. 5499, 2007.

[57] Q. Wang, J. Lu, and S. He, "Optimal design method of a low-loss broadband y branch with a multimode waveguide section," *Applied Optics*, vol. 41, no. 36, pp. 7644–7649, 2002.

[58] N. Riesen and J. D. Love, "Design of mode-sorting asymmetric y-junctions," *Applied Optics*, vol. 51, no. 15, pp. 2778–2783, 2012.

[59] J. B. Driscoll, R. R. Grote, B. Souhan, J. I. Dadap, M. Lu, and R. M. Osgood, "Asymmetric y junctions in silicon waveguides for on-chip mode-division multiplexing," *Optics Letters*, vol. 38, no. 11, pp. 1854–1856, 2013.

[60] K. Shirafuji and S. Kurazono, "Transmission characteristics of optical asymmetric y junction with a gap region," *Journal of lightwave technology*, vol. 9, no. 4, pp. 426–429, 1991.

[61] J. Love and A. Ankiewicz, "Purely geometrical coarse wavelength multiplexer/demultiplexer," *Electronics Letters*, vol. 39, no. 19, pp. 1385–1386, 2003.

[62] W. Henry and J. Love, "Asymmetric multimode y-junction splitters," *Optical and quantum electronics*, vol. 29, no. 3, pp. 379–392, 1997.

[63] W. Chen, P. Wang, and J. Yang, "Mode multi/demultiplexer based on cascaded asymmetric y-junctions," *Optics Express*, vol. 21, no. 21, pp. 25113–25119, 2013.

[64] S. Martínez-Garaot, S.-Y. Tseng, and J. Muga, "Compact and high conversion efficiency mode-sorting asymmetric y junction using shortcuts to adiabaticity," *Optics Letters*, vol. 39, no. 8, pp. 2306–2309, 2014.

[65] L. J. Fogel, "Evolutionary programming in perspective: The top-down view," *Computational intelligence: Imitating life*, 1994.

[66] Y. Li, "Genetic algorithms in search, optimization and machine learning genetic algorithms in search, optimization and machine learning, 1989," *JSME international journal. Series C, Mechanical systems, machine elements and manufacturing*, vol. 43, no. 2, pp. 335–341, 2000.

[67] I. Rechenberg, "Computational intelligence imitating life," *Zurada et al.[401], chapter Evolution strategy*, pp. 147–159, 1994.

[68] R. Eberhart and J. Kennedy, "A new optimizer using particle swarm theory," in *Micro Machine and Human Science, 1995. MHS'95., Proceedings of the Sixth International Symposium on*, pp. 39–43, IEEE, 1995.

[69] R. Kennedy, "J. and eberhart, particle swarm optimization," in *Proceedings of IEEE International Conference on Neural Networks IV, pages*, vol. 1000, 1995.

[70] R. Eberhart, R. Dobbins, and P. Simpson, "Computational intelligence pc tools, 1996."

[71] J.-R. Zhang, J. Zhang, T.-M. Lok, and M. R. Lyu, "A hybrid particle swarm optimization–back-propagation algorithm for feedforward neural network training," *Applied mathematics and computation*, vol. 185, no. 2, pp. 1026–1037, 2007.

[72] V. G. Gudise and G. K. Venayagamoorthy, "Comparison of particle swarm optimization and backpropagation as training algorithms for neural networks," in *Proceedings of the 2003 IEEE Swarm Intelligence Symposium. SIS'03 (Cat. No. 03EX706)*, pp. 110–117, IEEE, 2003.

[73] S. Mirjalili, S. Z. M. Hashim, and H. M. Sardroudi, "Training feedforward neural networks using hybrid particle swarm optimization and gravitational search algorithm," *Applied Mathematics and Computation*, vol. 218, no. 22, pp. 11125–11137, 2012.

[74] F. Wihartiko, H. Wijayanti, and F. Virgantari, "Performance comparison of genetic algorithms and particle swarm optimization for model integer programming bus timetabling problem," in *IOP Conference Series: Materials Science and Engineering*, vol. 332, p. 012020, IOP Publishing, 2018.

[75] D. C. Liu and J. Nocedal, "On the limited memory bfgs method for large scale optimization," *Mathematical programming*, vol. 45, no. 1-3, pp. 503–528, 1989.

[76] D. Sheppard, R. Terrell, and G. Henkelman, "Optimization methods for finding minimum energy paths," *The Journal of chemical physics*, vol. 128, no. 13, p. 134106, 2008.

[77] S. G. Nash and J. Nocedal, "A numerical study of the limited memory bfgs method and the truncated-newton method for large scale optimization," *SIAM Journal on Optimization*, vol. 1, no. 3, pp. 358–372, 1991.

[78] Lumerical, "Inverse design of y-branch," 2019. Available at https://apps.lumerical.com/inverse-design-y-branch.html.